Title

The Magnitude of Surface Ocean Acidification and Carbon Release During Eocene Thermal Maximum 2 (ETM-2) and the Paleocene-Eocene Thermal Maximum (PETM)

Journal

PALEOCEANOGRAPHY AND PALEOCLIMATOLOGY, 35(2)

ISSN

2572-4517

Authors

Harper, DT
Honisch, B
Zeebe, RE
et al.

Publication Date

2020

DOI

10.1029/2019PA003699

Peer reviewed

Paleoceanography and Paleoclimatology

RESEARCH ARTICLE
10.1029/2019PA003699

Key Points:
- Ocean acidification during Eocene Thermal Maximum 2 was more than half that of the PETM based on stable boron isotopes in foraminifera
- Our estimated carbon release for Eocene Thermal Maximum 2 is 2,600 to 3,800 Gt C
- Biogenic methane and/or organic C sources are required to achieve this flux and stay within limits of carbon isotope excursion and warming

Supporting Information:
- Supporting Information S1
- Supporting Information S2

Correspondence to:
D. T. Harper,
dtharper@ku.edu

Citation:
Harper, D. T., Hönisch, B., Zeebe, R., Shaffer, G., Haynes, L., Thomas, E., & Zachos, J. C. (2020). The magnitude of surface ocean acidification and carbon release during Eocene Thermal Maximum 2 (ETM-2) and the Paleocene-Eocene Thermal Maximum (PETM). *Paleoceanography and Paleoclimatology*, *35*, e2019PA003699. https://doi.org/10.1029/2019PA003699

Received 18 JUN 2019
Accepted 16 DEC 2019
Accepted article online 18 DEC 2019

The Magnitude of Surface Ocean Acidification and Carbon Release During Eocene Thermal Maximum 2 (ETM-2) and the Paleocene-Eocene Thermal Maximum (PETM)

D. T. Harper[1,2], B. Hönisch[3], R. E. Zeebe[4], G. Shaffer[5,6], L. L. Haynes[3], E. Thomas[7,8], and J. C. Zachos[1]

[1]Department of Earth and Planetary Sciences, University of California, Santa Cruz, CA, USA, [2]Now at Department of Geology, University of Kansas, Lawrence, KS, USA, [3]Department of Earth and Environmental Sciences, Lamont-Doherty Earth Observatory, Columbia University, Palisades, NY, USA, [4]School of Ocean and Earth Science and Technology, University of Hawaii at Manoa, Honolulu, HI, USA, [5]GAIA-Antarctica, Universidad de Magallanes, Punta Arenas, Chile, [6]Niels Bohr Institute, University of Copenhagen, Copenhagen, Denmark, [7]Department of Geology and Geophysics, Yale University, New Haven, CT, USA, [8]Department of Earth and Environmental Sciences, Wesleyan University, Middletown, CT, USA

Abstract Eocene Thermal Maximum 2 (ETM-2; 54.1 Ma) was the second largest Eocene hyperthermal. Like the Paleocene-Eocene Thermal Maximum (PETM), ETM-2 was characterized by massive carbon emissions and several degrees of global warming and thus can serve as a case study for assessing the impacts of rapid CO_2 emissions on ocean carbonate chemistry, biota, and climate. Marine carbonate records of ETM-2 are better preserved than those of the PETM due to more subdued carbonate dissolution. As yet, however, the magnitude of this carbon cycle perturbation has not been well constrained. Here, we present the first records of surface ocean acidification for ETM-2, based on stable boron isotope records in mixed-layer planktic foraminifera from two midlatitude ODP sites (1210 in the North Pacific and 1265 in the SE Atlantic), which indicate conservative minimum global sea surface acidification of −0.20 +0.12/−0.13 pH units. Using these estimates of pH and temperature as constraints on carbon cycle model simulations, we conclude that the total mass of C, released over a period of 15 to 25 kyr during ETM-2, likely ranged from 2,600 to 3,800 Gt C, which is greater than previously estimated on the basis of other observations (i.e., stable carbon isotopes and carbonate compensation depth) alone.

1. Introduction

The early Eocene was characterized by transient warming events, or hyperthermals, superimposed on a ~6 Myr warming trend (ca. 58 to 52 Ma; Littler et al., 2014; Lourens et al., 2005; Westerhold et al., 2018). The two largest hyperthermals were the Paleocene-Eocene Thermal Maximum (PETM; ca. 56 Ma) and Eocene Thermal Maximum 2 (ETM-2; ca. 54.1 Ma), with ETM-2 warming roughly half that of the PETM (Dunkley Jones et al., 2013; Harper et al., 2018; Sluijs et al., 2009; Stap et al., 2010). Both events are marked by rapid, large global $\delta^{13}C$ decreases (carbon isotope excursions, CIEs) in terrestrial and marine carbonates (e.g., up to 2‰ for ETM-2 and to 4‰ for the PETM, as measured in planktic foraminifera; e.g., Abels et al., 2012; Kennett & Stott, 1991; Koch et al., 1992; Lourens et al., 2005), evidence of intensification of the global hydrologic cycle (e.g., Baczynski et al., 2017; Harper et al., 2018; Kraus & Riggins, 2007; Nicolo et al., 2007; Schmitz & Pujalte, 2007; Zachos et al., 2003), and shifts in terrestrial and marine biota (e.g., Abels et al., 2012; D'Ambrosia et al., 2017; Jennions et al., 2015; Luciani et al., 2017; Petrizzo, 2007; Raffi et al., 2009; Sluijs & Brinkhuis, 2009; Thomas & Shackleton, 1996). Proposed carbon sources for the PETM include, but are not limited to, biogenic methane (e.g., Dickens et al., 1995), organic carbon (e.g., Bowen, 2013; DeConto et al., 2012; Kurtz et al., 2003), and volcanic emissions (Gutjahr et al., 2017). The prior two carbon sources are consistent with orbitally triggered mechanisms of carbon release for ETM-2 (e.g., Lourens et al., 2005; Zeebe & Lourens, 2019). Each source has a distinct stable carbon isotope signature (i.e., $\delta^{13}C$), so that the mass of carbon released can be inferred for each source type, if the full magnitude of the CIE is known (e.g., Kirtland Turner & Ridgwell, 2016).

Most importantly, hyperthermals are linked to global changes in ocean carbonate chemistry as evidenced by decreases in deep ocean $\%CaCO_3$ (Colosimo et al., 2006; Stap et al., 2009; Thomas & Shackleton, 1996; Zachos et al., 2005) and, for the PETM, independent records of surface ocean pH decrease (Babila et al., 2018;Gutjahr et al., 2017 ; Penman et al., 2014). Estimates of surface ocean acidification during the PETM are based on boron isotope values in planktic foraminiferal shells, which are directly controlled by ocean pH and closely related to atmospheric pCO_2 (Gutjahr et al., 2017; Penman et al., 2014). Stable boron isotope data, represented as $\delta^{11}B$, or the ratio $^{11}B/^{10}B$ normalized to a standard in permille (‰) notation, consistently indicate a global decrease in sea surface pH of ~0.3 units during the PETM (e.g., Babila et al., 2018; Gutjahr et al., 2017; Penman et al., 2014). These observations for the PETM have been used to constrain numerical simulations of the carbon cycle, thus the flux of carbon and pCO_2, and ultimately to estimate climate sensitivity. Model-based estimates of carbon release for the PETM range from 3,000 to 10,000 Gt C (e.g., Gutjahr et al., 2017; Shaffer et al., 2016; Zeebe et al., 2009), depending on the model used and paleoenvironmental constraints applied (e.g., CCD and pH). For the PETM, sediment records of the CCD support smaller magnitude release scenarios (e.g., Zeebe et al., 2009), whereas larger carbon release scenarios are required to match the magnitude of surface ocean acidification as estimated from foraminiferal $\delta^{11}B$ (e.g., Gutjahr et al., 2017).

Pelagic carbonate records of ETM-2 exhibit decreases in $\%CaCO_3$ of a smaller magnitude than during the PETM, suggesting proportionally reduced carbon emissions (Gibbs et al., 2012; Stap et al., 2009). However, there are no independent constraints on the marine carbonate system for ETM-2, limiting our ability to estimate the carbon fluxes and changes in atmospheric pCO_2 (e.g., Zeebe et al., 2009); here we address this deficiency. Simulations of ETM-2 carbon release with the LOSCAR model (Long-term Ocean-atmosphere-Sediment CArbon cycle Reservoir model; Zeebe, 2012) using a surface ocean CIE of −1.8‰ (Harper et al., 2018; Stap et al., 2010), sea surface warming of 2 to 4 °C (Harper et al., 2018), and ~150 m of Pacific ocean CCD shoaling (i.e., consistent with sediment records of Leon-Rodriguez & Dickens, 2010) suggest surface ocean acidification of just −0.05 pH units (Harper et al., 2018). Such simulations, however, may underestimate surface ocean acidification, because of the limited constraints on CCD shoaling during ETM-2 (i.e., Leon-Rodriguez & Dickens, 2010; Slotnick et al., 2015; Stap et al., 2009) and absence of independent constraints on pH.

Here we provide the first boron-based reconstructions of ETM-2 surface ocean acidification from midlatitude ODP Sites 1210 (North Pacific) and 1265 (SE Atlantic; Figure 1). To characterize the amount and source (i.e., $\delta^{13}C$; volcanic, methane, or organic) of carbon released during ETM-2, we compare our pH reconstructions and geochemical proxy records of climate and carbonate chemistry with carbon cycle-climate simulations applying two classes of models; the carbon cycle box model LOSCAR (Zeebe, 2012) and the Earth system model DCESS (Danish Center for Earth System Science; Shaffer et al., 2008). We use these models to explore the full range of ocean acidification scenarios possible for ETM-2. We also compare our ETM-2 pH reconstructions to estimates for the PETM from Site 1209, to investigate how differences in background conditions may have influenced the sensitivity of sea surface pH and temperature to carbon release.

2. Materials and Methods

2.1. Site Descriptions

We targeted foraminifera-rich pelagic sections from relatively shallow paleodepths to minimize the impacts of carbonate dissolution, from the southern high of Shatsky Rise in the North Pacific (Sites 1209 and 1210) and from Walvis Ridge in the South Atlantic (Site 1265), drilled during ODP Legs 198 and 208, respectively. ODP Sites 1209 (32°39.11′N, 158°30.36′E) and 1210 (32°13.41′N, 158°15.56′E) are in close proximity. We sampled both sites to demonstrate reproducibility and to provide enough planktic foraminiferal material. Paleogeographic reconstructions (paleolatitude = ~28°N; van Hinsbergen et al., 2015), place early Eocene Shatsky Rise in the subtropical North Pacific gyre (Figure 1), where large-scale ocean vertical mixing was unlikely. Sites 1209 and 1210 were positioned at ~1,900- and ~2,100-m paleo-water depth, respectively (Takeda & Kaiho, 2007). ODP Site 1265 (28°50.10′S, 2°38.35′E) was located at a paleolatitude of ~42°S (van Hinsbergen et al., 2015; Figure 1) and a paleodepth of ~1,850 m during the early Eocene (Zachos et al., 2004). Benguela-type coastal upwelling probably did not extend to Site 1265, but some vertical mixing cannot

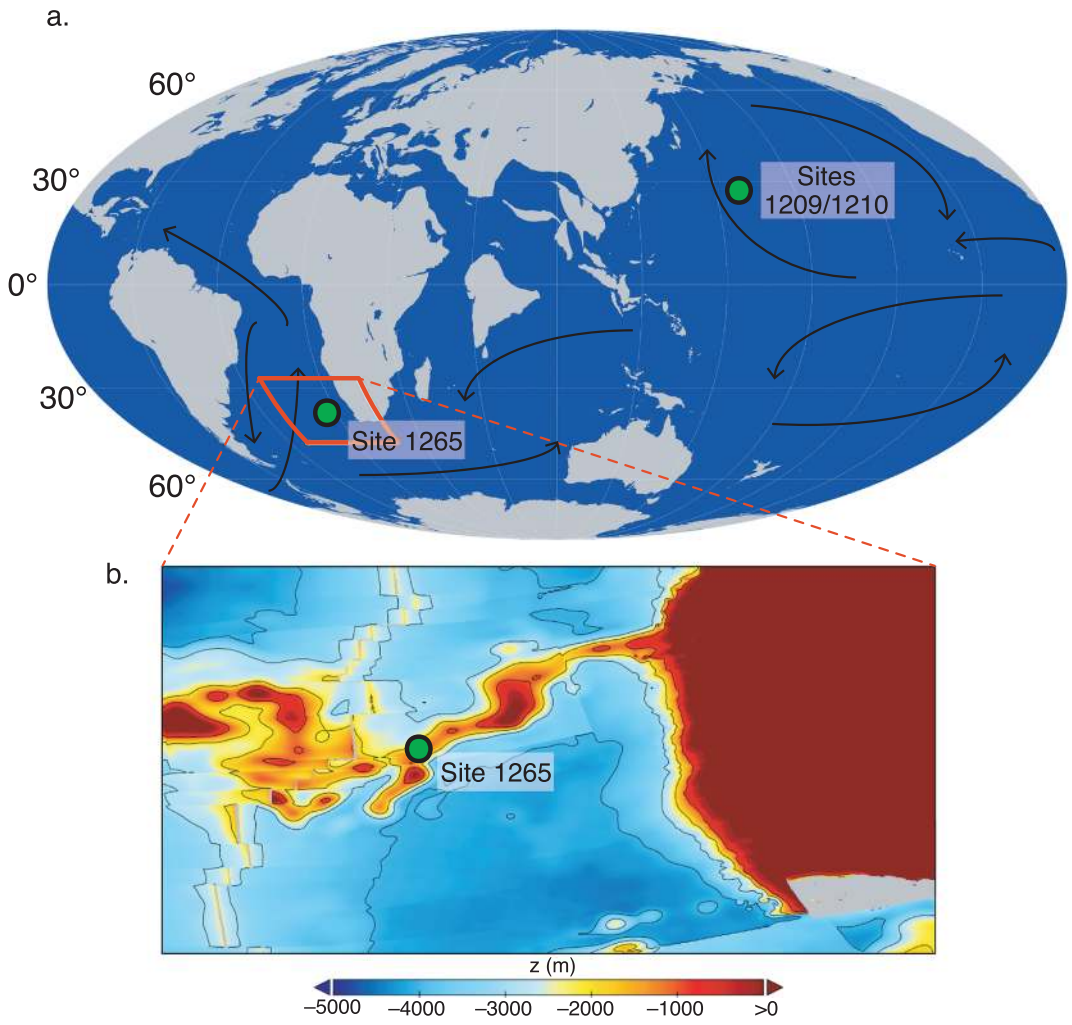

Figure 1. (a) Map showing ODP Site (1209/1210 and 1265) locations at 54 Ma (van Hinsbergen et al., 2015) and coastline reconstruction of Matthews et al. (2016). Black arrows indicate approximate surface ocean circulation during the early Eocene following Huber and Caballero (2003). Red box approximates the extent of the paleobathymetric map. (b) Paleobathymetry of Walvis Ridge region circa 60 Ma redrawn from Pérez-Díaz and Eagles (2018) with approximate location of Site 1265 indicated.

be ruled out (e.g., Kucera et al., 1997), given its paleobathymetry (i.e., located on a ridge; Figure 1) and the observation of differential warming by depths during ETM-2 (Jennions et al., 2015).

The planktic foraminifera are partially but uniformly recrystallized over the length scale of ETM-2 (Figures S1 and S2 in the supporting information); thus, some geochemical parameters, specifically absolute $\delta^{18}O$, are clearly compromised (e.g., Edgar et al., 2015; Stap, Lourens, van Dijk, et al., 2010). However, in theory, major and minor trace element concentrations, specifically Mg/Ca and B/Ca, should not change significantly in these relatively closed (i.e., low water/rock) systems (Edgar et al., 2015; Kozdon et al., 2013). Indeed, baseline and peak PETM Mg/Ca and B/Ca values from Site 1209 (i.e., Penman et al., 2014; Zachos et al., 2003) are consistent with values from siliciclastic sections such as Bass River, where foraminifera are pristine (i.e., Babila et al., 2016).

2.2. Analytical Methods

Bio- and magneto-stratigraphic evidence (Bralower et al., 2002) places ETM-2 in Core section 198-1210B-19H-6. To verify and determine the precise location of the CIE, a bulk carbonate $\delta^{13}C$ record was generated at ~2-cm resolution. Analyses were carried out via Isotope Ratio Mass Spectrometry (IRMS) using a Thermo

MAT 253 coupled to a Kiel IV carbonate device at the University of California, Santa Cruz. Additionally, samples were collected at 1- to 2-cm intervals and then washed and sieved to remove material <63 μm in preparation for foraminiferal identification for stable isotope and trace element analysis. ETM-2 was previously documented at ODP Sites 1209 (e.g., Gibbs et al., 2012) and 1265 (Lourens et al., 2005). Samples from Sites 1209 and 1265 were similarly washed and sieved prior to foraminiferal identification.

For the $\delta^{13}C/\delta^{18}O$ analysis of foraminifera, specimens were briefly sonicated in DI, rinsed in methanol, and dried in a 40 °C vacuum oven for 6 to 12 hr before analysis via IRMS. Analytical error for $\delta^{13}C$ and $\delta^{18}O$ (i.e., ±0.1‰ and ±0.16‰, respectively; 2RSD) is based on the long-term reproducibility of consistency standards (i.e., Carrara Marble). For major, minor, and trace element (e.g., B/Ca and Mg/Ca) analysis, 10 to 20 specimens of the mixed-layer planktic foraminifera species *Acarinina soldadoensis* were picked from the 250- to 355-μm-size fraction, lightly crushed, and cleaned, following the oxidative-reductive cleaning procedures of Martin and Lea (2002). Samples were then dissolved in 0.075N Optima grade HNO_3 and analyzed on a Thermo Element XR Inductively Coupled Plasma Mass Spectrometer (ICPMS) following the methodology of Brown et al. (2011). We screened trace element samples for clay contamination by measuring Al/Ca and used a similar cleaning strategy during $\delta^{11}B$ sample preparation (details below). Analytical error for minor and trace element ratios is ±7% for B/Ca and ±3% for Mg/Ca (2SD), as computed using the long-term reproducibility of in-house solution consistency standards. Splits of the same samples were analyzed for $\delta^{13}C$ and $\delta^{18}O$ via IRMS prior to oxidative and reductive cleaning. We include the bulk carbonate wt.% and $\delta^{13}C$, planktic Mg/Ca, and planktic and benthic $\delta^{13}C$ and $\delta^{18}O$ data from ODP Sites 1209 and 1265 of McCarren (2009), Stap et al. (2009); Stap, Lourens, Thomas, et al. (2010), Gibbs et al. (2012), and Harper et al. (2018).

Stable boron isotopes ($\delta^{11}B$) were measured by negative thermal ionization mass spectrometry following Hönisch et al. (2009), on samples of 90 to 160 individuals of *A. soldadoensis* from Sites 1210 and 1265. The $\delta^{11}B$ samples were picked from the 250- to 355-μm size fraction and crushed and cleaned to remove clays and organic and adsorbed contaminants following Barker et al. (2003). Cleaned material was dissolved in 2N Optima grade hydrochloric acid just before analysis, and 3 to 10 replicate aliquots of the sample solution containing ≥1 ng boron were loaded onto outgassed zone-refined rhenium filaments, along with 1 μl of boron-free seawater to enhance ionization. Analyses were done on a Thermo TRITON thermal ionization mass spectrometer in negative mode (N-TIMS) at the Lamont-Doherty Earth Observatory. Individual replicates were rejected if they fractionated excessively (i.e., >1‰) over the ~40 min of acquisition. Data uncertainty is reported as the larger of either the standard error (2SE) of acceptable replicate analyses or the 2SE of an equal number of repeat measurements of an in-house standard of NIST 951 precipitated in $CaCO_3$ matrix (vaterite; Foster et al., 2013). Planktic $\delta^{11}B$ data for the PETM were collected on the genus *Morozovella* (e.g., Gutjahr et al., 2017; Penman et al., 2014), but this genus is rare in the ETM-2 interval. To compare ETM-2 records to the PETM and constrain species offsets, we analyzed samples of PETM *A. soldadoensis* from the same intervals as *M. velascoensis* $\delta^{11}B$ data from ODP Site 1209 (Penman et al., 2014).

2.3. LOSCAR Simulations

LOSCAR has been used extensively to simulate variability of the carbon cycle in the past, particularly over the late Paleocene-early Eocene (e.g., Komar et al., 2013; Zeebe et al., 2017) and the PETM (e.g., Zeebe et al., 2009). LOSCAR carbon cycle simulations of ETM-2 were performed using a combination of carbon sources (i.e., biogenic methane and organic carbon) and fluxes, with sensitivity parameters for the effect of Mg^{2+}, Ca^{2+}, and SO_4^{2-} on equilibrium constants from Zeebe and Tyrrell (2019). The primary simulations include warming-induced shifts in shallow- to intermediate-depth remineralization of organic carbon (e.g., Matsumoto, 2007; Zeebe, 2013), and other model aspects are described in Zeebe (2012). We present three emission scenarios based on the orbitally tuned age models of Stap et al. (2009) and Westerhold et al. (2017), which constrain the CIE onset to 25 ± 5 kyr and 15 ± 5 kyr, respectively. We define the CIE onset as the depth at which planktic $\delta^{13}C$ continuously decreases until reaching the peak-CIE and therefore exclude the small excursion just prior to the rapid $\delta^{13}C$ decline, included as part of the ETM-2 CIE by Stap et al. (2009). Our definition of onset is consistent with the observation that there was no significant temperature change below the onset depth interval (e.g., Harper et al., 2018).

In our LOSCAR simulations, 2,600 Gt C with $\delta^{13}C$ of −37.5‰ is emitted consisting of a mixture of 1,300 Gt C with $\delta^{13}C$ of −25‰ (to simulate the release of organic carbon, C_{org}) and 1,300 Gt C with $\delta^{13}C$ of −50‰

(i.e., representing biogenic methane as proposed by Lourens et al., 2005). In the first two simulations (i.e., 15 and 25 kyr C release scenarios), the baseline atmospheric pCO_2 (ca. 54.1 Ma) is set at 1,600 μatm consistent with Anagnostou et al. (2016) (i.e., 1,400 ± 470 μatm at 53.2 Ma). The initial pCO_2 of the LOSCAR simulations is higher than that of Harper et al. (2018; i.e., 1,600 vs. 1,000 μatm), thus allowing for a larger mass of carbon (about twice) to be released for the same CIE, motivated in part to match the ETM-2 pH anomaly. Such a scenario likely requires a mixture of isotopically depleted and enriched carbon sources (e.g., methane plus organic carbon; $\delta^{13}C$ of −50‰ and −25‰, respectively) to achieve the observed CIE. The combined 2,600 Gt C are released over 15 kyr, and 25 kyr, at constant rates, with the aim to match observed rates and magnitudes of change in the CCD (Leon-Rodriguez & Dickens, 2010; Slotnick et al., 2015; Stap et al., 2009), $\delta^{13}C$ (Stap et al., 2010; Harper et al., 2018), and proxy-based estimates of ΔSST and pH (this study). Carbon is removed as C_{org} (−25‰) over 75 and 85 kyr for the 25 and 15 kyr release simulations, respectively, simulating the eccentricity paced (i.e., 100 kyr) release and storage of organic carbon as reflected in the duration of the CIE (Lourens et al., 2005; Zeebe & Lourens, 2019). Thus, LOSCAR neutralizes the carbon cycle perturbation through organic carbon burial and silicate weathering feedback.

To determine the sensitivity of carbonate chemistry and pH to background state, we also include one LOSCAR simulation that matches the initial conditions and emission scenario of one of the DCESS simulations (i.e., 2,600 Gt C with $\delta^{13}C = -37.5‰$ released over 20 kyr; initial atmospheric $pCO_2 = 1{,}050$ μatm, and initial Pacific surface pH = 7.68). In this simulation organic carbon (−25‰) is removed over 80 kyr following the initial release (i.e., similar to our primary simulations). We do not include warming-induced shifts in shallow- to intermediate-depth remineralization of organic carbon to consistently compare this LOSCAR simulation to DCESS.

2.4. DCESS Simulations

To better represent model uncertainties in model predictions for a range of possible carbon release scenarios, we applied a second model to run parallel simulations of ETM-2, DCESS, which differs from LOSCAR in terms of spatial resolution and included biogeochemical processes. The DCESS climate and carbon cycle model is a low-order Earth system model that features modules for the atmosphere, ocean, ocean biosphere, ocean sediment, land biosphere, and lithosphere (Shaffer et al., 2008). The model provides fast calculations due to the limited horizontal resolution (e.g., two ocean zones). However, unlike LOSCAR, inclusion of features such as heat and freshwater cycling, and a land biosphere allows for climate simulation. DCESS has been used to estimate changes in atmospheric pCO_2 during the PETM (Shaffer et al., 2016), and here we use the model to calculate pre-event initial conditions for the PETM and ETM-2 (Table S1), and to simulate ETM-2 carbon release. Consistent with recent mineralogical constraints for the Early Eocene Climate Optimum (minimum atmospheric pCO_2 between 680 and 1,260 μatm; Jagniecki et al., 2015), the baseline atmospheric pCO_2 is set at 1,050 μatm.

Initial conditions (pre-ETM-2) were obtained for prescribed pCO_2 and ocean phosphate inventory (Table S1). In an iterative process, carbon inventories and initial weathering inputs were varied until steady state balances between weathering/volcanic inputs matched sediment burial outputs for carbonate carbon, noncarbonate carbon, and phosphorus. This process and other aspects of the adaption of the model to Paleocene-Eocene conditions are described in Shaffer et al. (2016). In the simulations, weathering rates are climate-dependent and ocean phosphate inventories are free to vary. The model does not include shelf carbonate production, and other model aspects are described in detail in Shaffer et al. (2008).

For our simulation, we release 2,600 Gt C with $\delta^{13}C$ of −37.5‰ over 20 kyr consistent with a mixture of organic and biogenic methane carbon sources. The release rate of carbon to the atmosphere is gradually increased during the first 5 kyr and decreased during the last 5 kyr of release, plateauing for ~10 kyr, which generates slightly smoothed decreases in $\delta^{13}C$ during the onset of ETM-2. Additionally, to test a range of possible carbon sources, we include two more extreme C release scenarios for ETM-2 representing carbon sources more enriched in ^{13}C (pure C_{org} and volcanic CO_2): (1) 3,800 Gt C with $\delta^{13}C$ of −25‰ released over 20 kyr, and (2) 10,600 Gt C with $\delta^{13}C$ of −10‰ released over 20 kyr.

For DCESS simulations, drawdown of organic carbon is not forced, but recovery is driven by increased organic carbon burial resulting from enhanced phosphate delivery to oceans via increased continental weathering, in addition to the silicate weathering feedback. The initial conditions for the DCESS

simulations differ from those applied to our primary LOSCAR simulations, such that the simulations with both models span the range of pre-ETM-2 pCO_2 implied by different data constraints (Anagnostou et al., 2016; Jagniecki et al., 2015). Thus, this approach provides a broad range of possible scenarios for comparison with our data-derived results.

3. Results

3.1. Geochemical Proxy Records

ETM-2 occurs in Core section 1210B-19H-6, with a −0.8‰ CIE, similar in magnitude to that at Sites 1209 (−0.7‰ bulk carbonate CIE; Gibbs et al., 2012) and 1265 (−0.8‰ bulk carbonate CIE; Stap et al., 2009; Figure 2). Benthic $\delta^{13}C$ and $\delta^{18}O$ decreased during ETM-2 by 0.9‰ and 0.6‰, respectively (Figure 2). Planktic $\delta^{13}C$ decreased by 1.3‰ at Site 1210, similar to planktic CIEs at other sites (−1.1‰ at Site 1209 and −1.4‰ at Site 1265; Harper et al., 2018) (Figure 2). Baseline planktic Mg/Ca from Shatsky Rise sites show slightly higher pre-ETM-2 values than pre-PETM values (Penman et al., 2014; Zachos et al., 2003), suggesting long-term warming consistent with benthic $\delta^{18}O$ records (Figures 3 and 4). Remarkably, the ETM-2 baseline Mg/Ca is higher at Site 1265 than at Sites 1209 and 1210, despite its higher paleo-latitude. Site 1210 planktic Mg/Ca increased during ETM-2 from ~3.6 mmol/mol to ~4.5 mmol/mol (Figure 4), similar to absolute values and the magnitude of the increase at Site 1209. Site 1265 planktic Mg/Ca increased from ~3.8 to ~4.7 mmol/mol (Harper et al., 2018).

At all sites planktic (*A. soldadoensis*) B/Ca (Sites 1209, 1210, and 1265) and $\delta^{11}B$ (Sites 1210 and 1265) decreased during the ETM-2 CIE (Figure 4). Site 1209 planktic B/Ca decreased from ~60 to ~40 μmol/mol (Figure 4). Coarse resolution B/Ca data from Site 1210, corresponding to samples analyzed for $\delta^{11}B$, mimic the higher resolution 1209 record (Figure 4). At Southeast Atlantic Site 1265 planktic B/Ca decreased during ETM-2 from ~44 to ~30 μmol/mol (Figure 4). Planktic $\delta^{11}B$ decreased by 1.1‰ (from 15.8‰ to 14.7‰) at Site 1210, and by 1.5‰ (from 15.5‰ to 14.0‰) at Site 1265 (Figure 4) during ETM-2. For comparison, *A. soldadoensis* $\delta^{11}B$ decreased by 1.6‰, from 15.4‰ to 13.8‰ across the PETM. The pre-event $\delta^{11}B$ baseline is higher for ETM-2 than for the PETM, suggesting higher baseline pH and/or $\delta^{11}B_{sw}$ during the event (discussed below).

3.2. Reconstructing Sea Surface Temperatures for ETM-2 and the PETM

Absolute temperature records for ETM-2 are reconstructed using planktic Mg/Ca from Sites 1209 and 1210, and 1265 (Harper et al., 2018) and early Eocene Mg/Ca estimates of seawater of $Mg/Ca_{sw} = 2.24$ mol/mol (Evans et al., 2018). Coarse resolution Mg/Ca data from Site 1210 generally agree with data from Site 1209, although the two records slightly diverge during the CIE recovery. To calculate temperature, we apply a Mg/Ca-SST calibration sensitivity (i.e., the pre-exponential and exponential calibration constants, or B and A values, respectively) consistent with Eocene seawater conditions (i.e., $A = 0.075$ following Evans et al., 2016, and $B = 0.38$; Anand et al., 2003, with added Mg/Ca_{sw} adjustments of Evans & Müller, 2012). Further, planktic Mg/Ca data are adjusted for the pH-effect on Mg/Ca using site-specific $\delta^{11}B$-based pH estimates (but excluding two $\delta^{11}B$ samples with less than three replicates, orange symbols in Figure 4l), and following the linear pH-adjustment of Evans et al. (2016). To account for the interdependence of temperature and pH calculations from the Mg/Ca and $\delta^{11}B$ proxies, we first compute temperature without pH-adjustment to determine $\delta^{11}B$-based pH and then use this pH estimate to adjust the Mg/Ca data (i.e., we recalculate SST with the pH effect). This is then followed by a final pH calculation using this adjusted temperature estimate and a final temperature calculation with the final pH estimate. This strategy minimizes the additional mutual influence of temperature and pH with each iteration. Overall, the pH-adjustment of temperature estimates decreases peak-CIE warming by less than 0.5 and 0.3 °C for the PETM and ETM-2, respectively. Using non-pH-adjusted SSTs for calculation of pH from $\delta^{11}B$ dampens the negative pH excursion during ETM-2 by less than 0.015 pH units for Sites 1210 and 1265 (i.e., the effect is smaller than the respective ±0.038 and ±0.084 average propagated analytical uncertainty in pH estimates for these sites). Our pH correction aligns the SST estimates for Shatsky Rise and Walvis Ridge, because pre-ETM-2 $\delta^{11}B$ and B/Ca (i.e., pH) are lower at Walvis Ridge than at Shatsky Rise.

Both midlatitude ETM-2 SST records indicate similar pre-event baseline and peak-CIE temperatures of ~35 and ~37.5 °C, respectively (Figure 4). To obtain an absolute SST uncertainty envelope (i.e., gray lines in

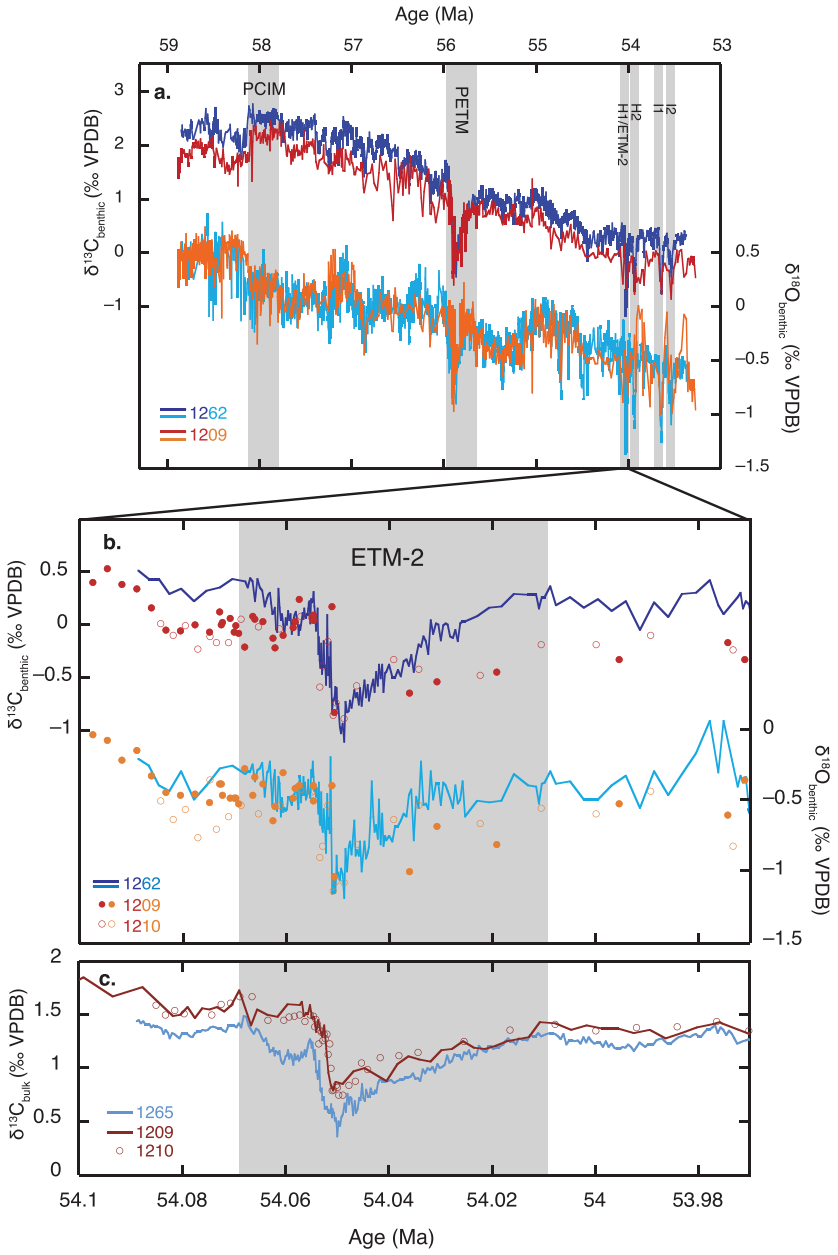

Figure 2. (a) Late Paleocene-Early Eocene (LPEE) benthic $\delta^{13}C$ and $\delta^{18}O$ records from ODP Sites 1209 (red and orange) and 1262 (blue and light blue), compiled by and placed on the age model of Westerhold et al. (2018) and Barnet et al. (2019), respectively. (b) Benthic $\delta^{13}C$ and $\delta^{18}O$ records during Eocene Thermal Maximum 2 (ETM-2) from ODP Sites 1209 (closed red and orange circles; Harper et al., 2018; McCarren, 2009), 1210 (open red and orange circles; this study), and 1265 (blue and light blue lines; Stap, Lourens, Thomas, et al., 2010). (c) Bulk carbonate $\delta^{13}C$ during ETM-2 from Sites 1209 (burgundy line; Gibbs et al., 2012), 1210 (open burgundy circles; this study), and 1265 (light purple line; Stap et al., 2009). Panels b and c are placed on the Ypresian age model of Westerhold et al. (2017), consistent with the Late Cretaceous-Early Eocene age model of Barnet et al. (2019).

Figures 3 and 4), we propagate analytical uncertainty in Mg/Ca (i.e., ±3% 2SD), apply the Mg/Ca-temperature calibration uncertainty of Anand et al. (2003) in the pre-exponential constant (B value = 0.38 ± 0.02 adjusted for Mg/Ca_{sw} of 2.24 mol/mol), and prescribe a range of exponential constants following Evans et al. (2016; A values = 0.075 ± 0.005) consistent with early Eocene Mg/Ca_{sw} of 2.24 mol/mol (Evans et al., 2018). In propagating the SST uncertainty, we include the $\delta^{11}B_{calcite}$ versus $\delta^{11}B_{borate}$ calibration slope uncertainty (±0.07 for *A. soldadoensis* and ±0.08 for *M. velascoensis*; Hönisch et al., 2019)

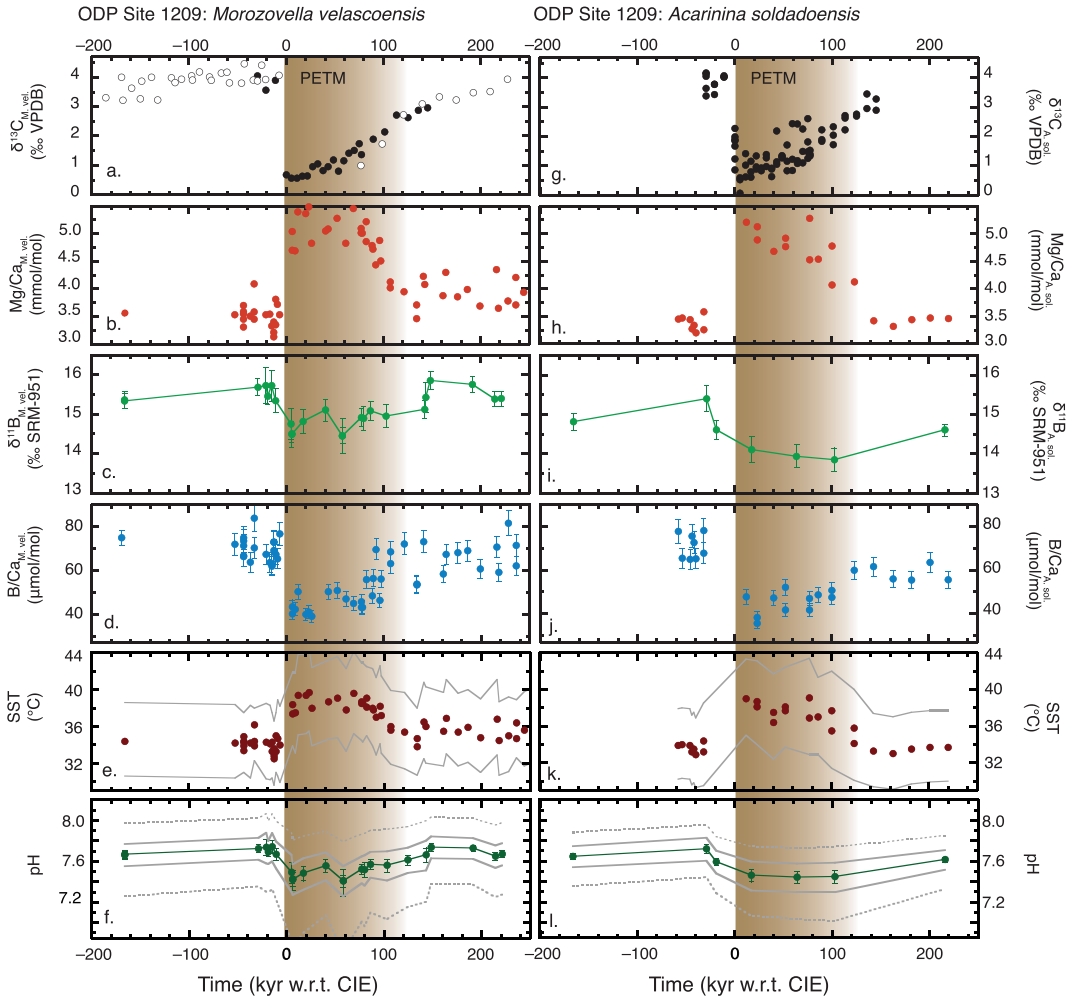

Figure 3. ODP Site 1209 geochemical data from planktic foraminifera *Morozovella velascoensis* (panels a–d; Penman et al., 2014; open circle $\delta^{13}C$ = this study) and *Acarinina soldadoensis* (panels g–j; Penman et al., 2014; $\delta^{11}B$ = this study) during the Paleocene-Eocene Thermal Maximum (PETM). We compute sea surface temperature (SST) from Mg/Ca (panels e and k; this study) and pH from $\delta^{11}B$ (panels f and l; this study). pH uncertainties reflect $\delta^{11}B$ analytical error (green error bars), propagated errors in measured $\delta^{11}B$, SST, sea surface salinity, and $\delta^{11}B_{sw}$ (solid gray lines); dashed gray lines additionally include the $\delta^{11}B_{calcite}$ versus $\delta^{11}B_{borate}$ *T. sacculifer* (applied to *M. velascoensis*) and *O. universa* (applied to *A. soldadoensis*) calibration uncertainties after Hönisch et al. (2019). Data are placed on the relative age model of Röhl et al. (2007).

and its effect on site-specific pH estimates. Further, we include non-pH adjusted Mg/Ca-based SST ranges within our uncertainty bounds.

3.3. pH From $\delta^{11}B_{foram}$

Mixed-layer pH is calculated from $\delta^{11}B_{foram}$ following Hönisch et al. (2019), using routines of Zeebe and Wolf-Gladrow (2001). Site 1209 PETM pH is recalculated using *M. velascoensis* $\delta^{11}B$ data of Penman et al. (2014). The pH calculations include the effects of pressure (i.e., Millero, 1995) temperature and salinity on the boric acid/borate stoichiometric equilibrium constant (i.e., pK^*_B), but not the effect of major ion seawater composition (i.e., seawater $[Mg^{2+}]$ and $[Ca^{2+}]$) on pK^*_B, which is generally considered to be minor (Hershey et al., 1986). For example, compared with modern, early Eocene major ion concentrations (i.e., lower Mg^{2+} and higher Ca^{2+}) would tend to raise pK^*_B (Hain et al., 2015), but this effect results in <0.01 pH unit reduction in our pH anomaly estimates. We use absolute temperature from pH-adjusted Mg/Ca-based SST (Figures 3 and 4) and implement conservative sea surface salinization for both PETM (from 35 to 37 ppt during peak SSTs) and ETM-2 (from 35 to 36 ppt during peak SSTs) pH calculations (e.g., Harper et al., 2018;

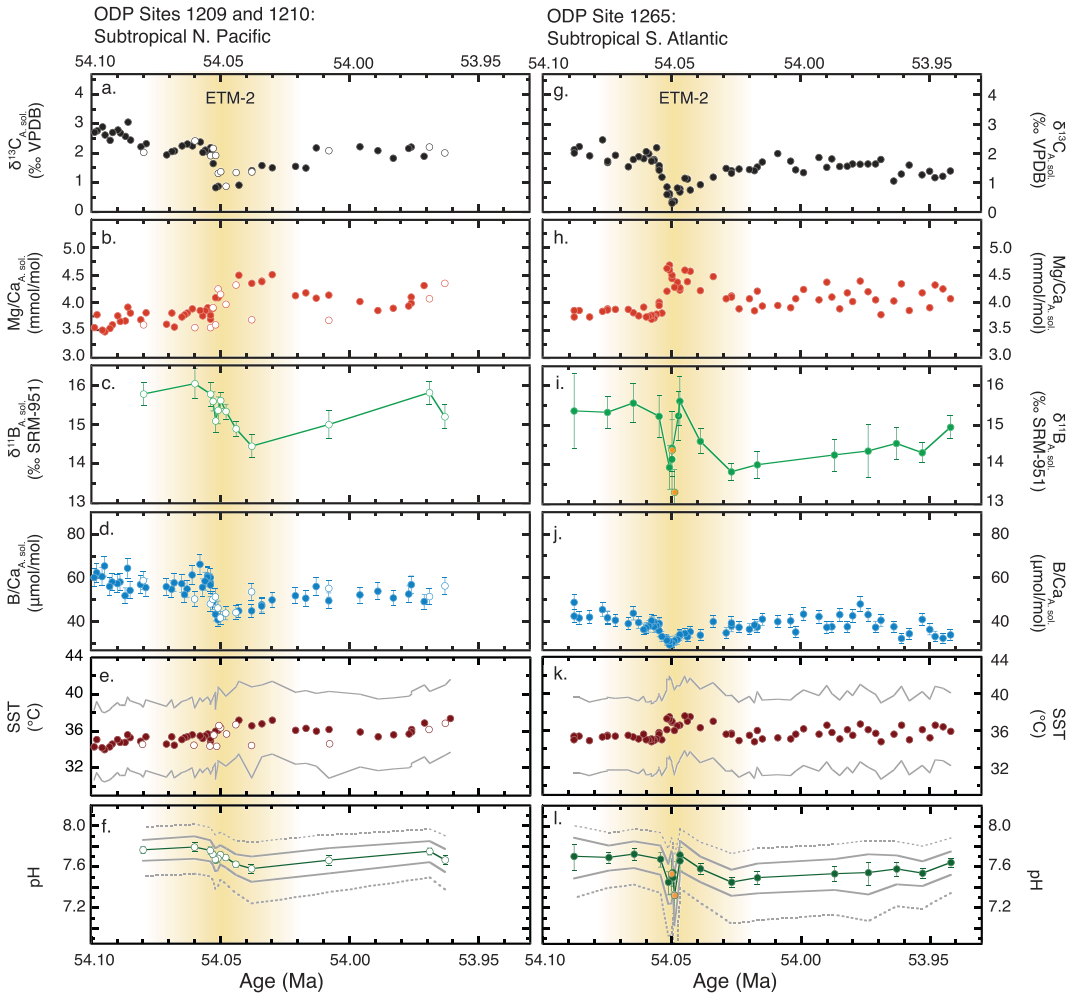

Figure 4. Geochemical data from planktic foraminifera *Acarinina soldadoensis* during Eocene Thermal Maximum 2 (ETM-2). Note that *y* ranges are the same as in Figure 3, to allow quantitative visual comparison of the two events. Panels a–d show data from ODP Sites 1209 (closed circles; this study; Harper et al., 2018) and 1210 (open circles; this study). Panels g–j show data from ODP Site 1265 (this study; Harper et al., 2018). Sea surface temperature is computed from Mg/Ca (panels e and k) and pH from $\delta^{11}B$ (panels f and l). Orange symbols in panels i and l indicate data with <3 N measurements. pH uncertainties reflect $\delta^{11}B$ analytical error as described in Figure 3. Data are placed on the absolute age model of Westerhold et al. (2017).

Zachos et al., 2003). Adding 2 ppt salinization during the hyperthermals results in an amplification of acidification (i.e., ΔpH) of less than 0.015 pH units.

For our PETM and ETM-2 pH calculations, we use the early Eocene $\delta^{11}B$ of seawater ($\delta^{11}B_{sw}$) estimate of Anagnostou et al. (2016; i.e., 38.75 ± 0.15‰; the early Eocene value they determined under assumptions most consistent with $\delta^{11}B_{foram}$–$\delta^{11}B_{borate}$ sensitivities applied below). We apply the aqueous boron isotope fractionation (i.e., $\varepsilon_{B3\text{-}B4}$ = 27.2‰) of Klochko et al. (2006). Both *A. soldadoensis* and *M. velascoensis* are thought to have hosted algal photosymbionts based on $\delta^{13}C$-size relationships, thus likely resided in the mixed-layer (D'Hondt et al., 1994). To convert their $\delta^{11}B$ data to $\delta^{11}B_{borate}$ (and hence pH), we use the different $\delta^{11}B_{calcite}$ versus $\delta^{11}B_{borate}$ sensitivities of two modern symbiont-bearing species for the two extinct species based on their ecological characteristics. We apply the sensitivity of modern symbiont-bearing, surface-dwelling *T. sacculifer* to *M. velascoensis* (m = 0.73 ± 0.08; Dyez et al., 2018; Sanyal et al., 2001), and modern symbiont-bearing, slightly deeper surface-dwelling *O. universa* (m = 0.99 ± 0.07; Hönisch et al., 2019, refit of Henehan et al., 2016) to *A. soldadoensis*. We calibrate the species-specific $\delta^{11}B_{foram}$ intercept to an initial pre-PETM pH of 7.72 (i.e., intercept c = 0.37 for *A. soldadoensis* and c = 4.57 for *M. velascoensis*). The application

of two different modern sensitivities minimizes the difference between the $\delta^{11}B$-based *M. velascoensis* and *A. soldadoensis* PETM pH records at Site 1209. In contrast, application of the average photosymbiotic foraminifera multispecies sensitivity of Hönisch et al. (2019; i.e., m = 0.68 ± 0.04) results in slightly larger pH differences between the two species (Figure S3).

Baseline PETM pH is obtained from the DCESS simulation with an initial pre-PETM atmospheric pCO_2 of 800 μatm (i.e., Shaffer et al., 2016). We attribute the interspecies offset (difference in *c* values) and sensitivity differences (difference in *m* values) to small differences in depth habitat (i.e., 40 m for *M. velascoensis* and 70 m for *A. soldadoensis*), consistent with $\delta^{18}O$ and Mg/Ca, which suggest slightly cooler temperatures for *A. soldadoensis* (e.g., Zachos et al., 2003), and therefore prescribe slightly different pressure values to pH calculations for each species.

Seawater pH uncertainty is calculated and displayed (Figures 3 and 4) according to three sets of considerations: (1) analytical 2 SE uncertainty from $\delta^{11}B$ measurements (green error bars); (2) propagated uncertainty including analytical 2 SE on $\delta^{11}B$, SST (gray error bars in Figures 3 and 4), sea surface salinity (i.e., ±1 ppt, given uncertainty in midlatitude sea surface salinization; Zachos et al., 2003; Harper et al., 2018), and reported uncertainty in $\delta^{11}B_{sw}$ (i.e., 38.75 ± 0.15; Anagnostou et al., 2016; solid gray lines); and 3) including all above uncertainties, with the additional $\delta^{11}B_{calcite}$ versus $\delta^{11}B_{borate}$ calibration slope uncertainty of Hönisch et al. (2019; i.e., ±0.08 for *M. velascoensis* and ±0.07 for *A. soldadoensis*; dashed gray lines). We include all three uncertainty bounds in Figures 3 and 4, and the prior two uncertainties in our interpretation.

3.4. Carbon Release Simulations

Our ETM-2 carbon flux scenarios with LOSCAR-based estimates of initial conditions, in which 1,300 Gt C (−50‰ $\delta^{13}C$) + 1,300 Gt C (−25‰ $\delta^{13}C$) are released, result in increased atmospheric pCO_2 from 1,600 μatm to 2,400 and 2,460 μatm for the 25 and 15 kyr release scenarios, respectively (Figure 5). Assuming a climate sensitivity of 4 °C per doubling of atmospheric pCO_2 (i.e., consistent with Dunkley Jones et al., 2010, and the lower end of estimates by Shaffer et al., 2016, for the PETM), generates warming of 2.0 to 2.2 °C (Figure 6). Surface $\delta^{13}C$ in the Pacific (Figure 5) and Atlantic (Figure S4) decreases by –2.1‰ for both 25 and 15 kyr release scenarios. The simulations generate pH excursions of −0.12 and −0.13 pH units for the 25 and 15 kyr release scenarios, respectively (Figure 5). The Pacific and Atlantic CCD shoal by 200 and 300 m (Figures 5 and S4), respectively, and DIC increases in both release scenarios by ~120 μmol/kg (Figure S3). A third LOSCAR simulation (with initial conditions set to match DCESS), in which 2,600 Gt C is released over 20 kyr, results in a similar response (i.e., pH decrease and temperature anomaly, and CCD shoaling of 300 and 450 m in the Pacific and Atlantic, respectively; Figures 5 and S8) as the 2,600 Gt C DCESS simulation.

The CIEs in all three DCESS simulations (2,600, 3,800, and 10,600 Gt carbon release scenarios) are similar to those of LOSCAR as well as observations (CIEs = ~–2‰; Figures 5 and S7). Atmospheric pCO_2 increases from 1,050 μatm to 1,470 and 1,690 μatm for the 2,600 and 3,800 Gt C simulations, respectively (Figure 5). Assuming climate sensitivity of 4 °C per CO_2 doubling, modeled surface temperatures increased by 1.8 and 2.5 °C, respectively (Figure 6). The 2,600 Gt C scenario results in a decrease in surface pH (−0.12 pH units) similar to that of the two LOSCAR simulations, whereas the 3,800 Gt C scenario results in a −0.17 pH unit decrease. Similarly, the CCD shoaling is 200 m in the 2,600 Gt C simulation compared to 250 m with 3,800 Gt C (Figure 5). The most extreme DCESS scenario with 10,600 Gt C release results in an increase in pCO_2 from 1,050 to 3,160 μatm, a surface ocean pH-decrease of −0.38, surface ocean warming of 5.8 °C, and >500 m of global mean CCD shoaling (Figure S7).

3.5. Records of Planktic B/Ca

B/Ca of planktic foraminifer shells is a promising proxy for surface ocean carbonate chemistry (Allen & Hönisch, 2012; Yu et al., 2007), as the relative abundance of borate ion in seawater covaries with pH (Hershey et al., 1986) and foraminifera are thought to only incorporate the borate ion chemical species (Hemming & Hanson, 1992), though its exact systematics are still under investigation (e.g., Allen et al., 2011; Babila et al., 2014; Haynes et al., 2017; Henehan et al., 2015; Hönisch et al., 2019; Salmon et al., 2016). We therefore interpret DIC from PETM and ETM-2 planktic B/Ca records (in conjunction with borate from estimated pH) following the proxy-development advances of Haynes et al. (2017) in the supporting information (Figures S9 and S10) and focus here on calculating the magnitudes of the pH excursion and warming using planktic $\delta^{11}B$ and Mg/Ca, with the aim of constraining numerical simulations to estimate

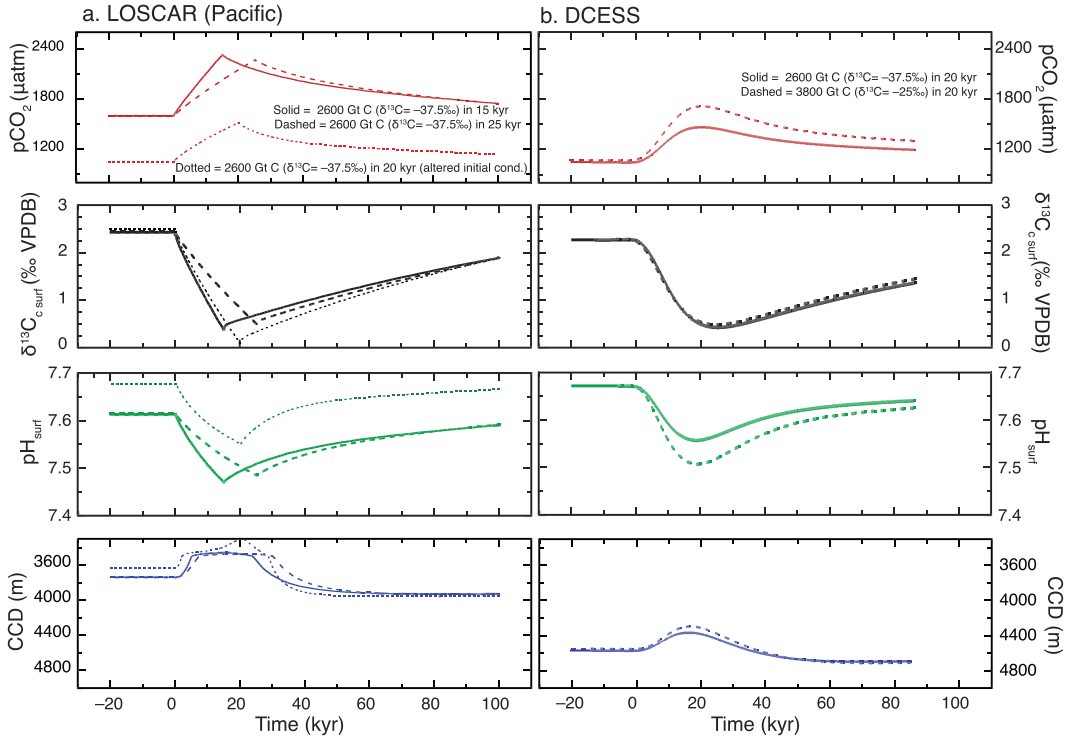

Figure 5. Carbon cycle model output for LOSCAR (panel a) and DCESS (panel b) Eocene Thermal Maximum 2 (ETM-2) simulations. (a) For LOSCAR, 1,300 Gt organic C (−25‰) + 1,300 Gt biogenic methane C (−50‰) is released over 25 kyr (dashed lines), 20 kyr (dotted lines), and 15 kyr (solid lines), and output corresponds to low latitude to midlatitude Pacific Ocean. LOSCAR 20 kyr C release simulation excludes shifts in shallow to intermediate water depth organic C remineralization and includes adjustments to initial conditions for comparison to DCESS 2,600 Gt C release simulation (see also Figure S8). (b) For DCESS, 2,600 Gt mixed organic and biogenic methane C (−37.5‰; solid lines) and 3,800 Gt organic C (−25‰; dashed lines) is released over 20 kyr. DCESS $\delta^{13}C$ and pH outputs correspond to global mean surface ocean values, and CCD output corresponds to low to middle latitude ocean.

carbon release during ETM-2. The direction of B/Ca changes across PETM and ETM-2 records qualitatively agrees with the $\delta^{11}B$ records and therefore with ocean acidification across both events.

4. Discussion

4.1. ETM-2 and the PETM Warming

Our pre-event baseline temperature of ~35 °C and relative warming (i.e., +2 to 3 °C) across ETM-2 are comparable to records from other sites, using different proxies, and suggest globally uniform warming. High latitude TEX_{86} temperature records (e.g., Sluijs et al., 2009) and benthic $\delta^{18}O$ records (e.g., Stap, Lourens, Thomas, et al., 2010) suggest high-latitude pre-event temperatures of ~20 °C with 2 to 4 °C warming during the CIE. This implies that the full magnitude of the temperature signal is captured at all sites, consistent with weak polar amplification in response to GHG forcing in the absence of ice-albedo feedbacks (Kiehl & Shields, 2013). The uniformity between the warming at our midlatitude sites and that documented at high latitudes is consistent with the assumptions that mixed-layer photosymbiont bearing foraminifera did not migrate to deeper waters, nor that our midlatitude records were truncated by dissolution, which would have diminished the SST anomaly (Stap, Lourens, Thomas, et al., 2010).

To compare our SST estimates for ETM-2 to those of the PETM, we reconstruct absolute temperature for the PETM at ODP Site 1209 using foraminiferal Mg/Ca (*A. soldadoensis* and *M. velascoensis*; Penman et al., 2014), Mg/Ca_{sw} of 2.24 mol/mol consistent with the value applied to ETM-2, following the early Eocene estimates of Evans et al. (2018), and $\delta^{11}B$-based pH using our $\delta^{11}B_{A.\ soldadoensis}$ data and the $\delta^{11}B_{M.\ velascoensis}$ data of Penman et al. (2014). SST reconstructions indicate warming from an initial pre-PETM temperature of ~34

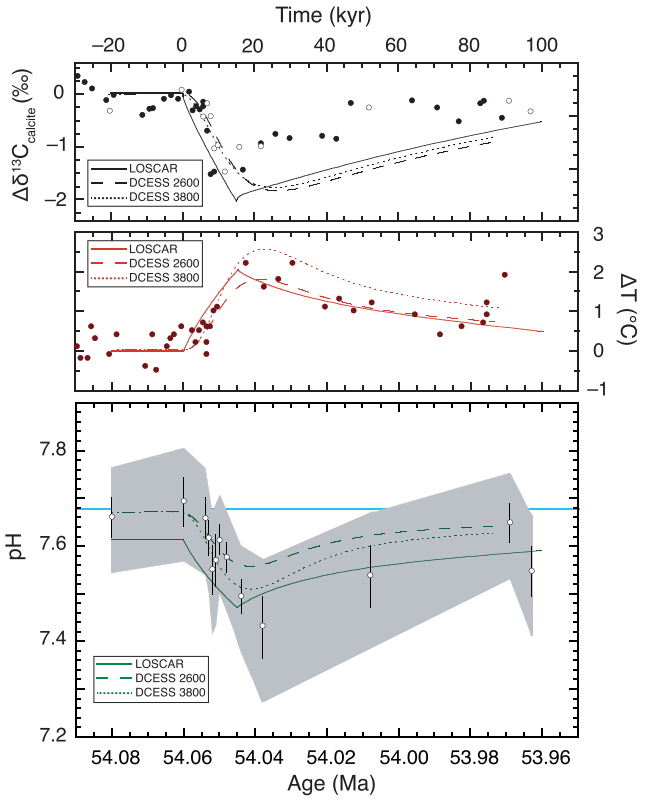

Figure 6. Geochemical data ($\Delta\delta^{13}C$) and interpretations (ΔSST and pH) from planktic foraminifera *Acarinina soldadoensis* during Eocene Thermal Maximum 2 (ETM-2) from Pacific ODP Site 1209 (closed circles) and 1210 (open circles). pH is calculated here by setting baseline pre-ETM-2 to DCESS-calculated pH = 7.68 (baseline pH = light blue line). This lower baseline pH results in amplification of the pH excursion (cf. Figure 4f). $\delta^{11}B$-based uncertainty in pH estimates indicated by black error bars (analytical uncertainty in $\delta^{11}B_{foram}$) and gray envelope (reflects propagated uncertainty in $\delta^{11}B_{foram}$, SST, salinity, and $\delta^{11}B_{sw}$). Data are placed on the age model of Westerhold et al. (2017). Superposed on geochemical data are LOSCAR and DCESS model outputs for the low to middle latitude Pacific surface ocean for three release scenarios: (1) 2,600 Gt C (−37.5‰) over 15 kyr LOSCAR simulation (solid line), (2) 2,600 Gt C (−37.5‰) over 20 kyr DCESS simulation (dashed line), and (3) 3,800 Gt C (−25‰) over 20 kyr DCESS simulation (dotted line).

to ~40 °C during the main CIE at Site 1209 (Figure 3) and are consistent with midlatitude TEX_{86}-based SST reconstructions from higher midlatitude sites, Bass River and Wilson Lake, which yield pre-PETM SSTs in the upper 20s (°C) and warming to the mid-30s (°C) during peak warmth (e.g., Sluijs et al., 2007).

4.2. Surface Ocean Acidification During ETM-2 and the PETM

We report ΔpH as the difference between pre-event baseline pH, and the minimum value constrained by $\delta^{11}B_{foram}$ including its associated uncertainty. Including the uncertainties in temperatures (i.e., gray SST lines in Figures 3 and 4), salinity (i.e., slight sea surface salinization ±1 ppt), and the reported error in $\delta^{11}B_{sw}$, the estimated range of acidification across ETM-2 is −0.20 +0.12/−0.13 and −0.26 +0.12/−0.14 pH units for Sites 1210 and 1265, respectively (Figure 4 and Table 1). Pre-PETM baseline pH is set to 7.72, calculated with DCESS using a pre-PETM pCO_2 of 800 μatm consistent with Shaffer et al. (2016). This results in a baseline ETM-2 (i.e., ETM-2 data > 54.052 Ma) pH of 7.78 and 7.71 for Sites 1210 and 1265, respectively (Figures 3 and 4; i.e., Shatsky sites pH increases due to the recorded rise in $\delta^{11}B_{foram}$ from post-PETM to pre-ETM-2). Our ΔpH does not include the two Site 1265 $\delta^{11}B$ values with <3N measurements (orange circles in Figure 4l), which agree with the ocean acidification trend recorded by other samples, but are analytically considered less reliable (e.g., Foster et al., 2013).

The increase in $\delta^{11}B_{foram}$ from post-PETM to pre-ETM-2 in the Pacific (this study) and Atlantic (this study; Penman et al., 2014) ocean basins (Figures 3 and 4) suggests a long-term increase in sea surface pH and/or $\delta^{11}B_{sw}$ following the PETM or a pH and/or $\delta^{11}B_{sw}$ increase directly preceding ETM-2. Whether the change happened more gradually (i.e., long-term) or more rapidly immediately before ETM-2 cannot be evaluated without a continuous $\delta^{11}B$ record between the two events. However, a long-term pH increase is contrary to expectations based on observations of the global decline in benthic $\delta^{18}O$ and $\delta^{13}C$, and shoaling CCD over the early Eocene (Figure 2), which generally have been interpreted to indicate global warming, likely due to increased atmospheric pCO_2 (Bijl et al., 2009; Littler et al., 2014; Westerhold et al., 2011; Westerhold et al., 2017; Zachos et al., 2001). Postevent observations of $\delta^{11}B$ (PETM and ETM-2; Gutjahr et al., 2017; this study; Penman et al., 2014) show lower values than pre-event $\delta^{11}B$, generally consistent with warming and higher atmospheric pCO_2 following hyperthermal recovery and leading up to peak warmth during the Early Eocene Climatic Optimum (EECO).

The average estimated pH decrease at Shatsky Rise during ETM-2 is more than half that estimated for the PETM (i.e., −0.20 +0.12/−0.13 for ETM-2 and −0.31 +0.14/−0.15 for PETM; Table 1), despite a proportionally larger difference between planktic CIEs (i.e., −3.5‰ and −1.3‰ for the PETM and ETM-2, respectively; Figures 3 and 4; Harper et al., 2018; Penman et al., 2014; Stap, Lourens, van Dijk, et al., 2010) and ΔSSTs (e.g., ~6 °C vs. ~2.5 °C sea surface warming for the PETM and ETM-2, respectively; Figures 3 and 4). Based on the relatively smaller CIE and reduced warming, we would expect a carbon cycle perturbation less than half that of the PETM, thus less than half the acidification for ETM-2 than for the PETM. The fact that our acidification estimates for both events are broadly within error suggests that there were additional influencing factors on pH.

One possible factor involves algal photosymbionts, which in planktic foraminifera elevate $\delta^{11}B$ and $\delta^{13}C$ values relative to those in symbiont-barren species (e.g., Hönisch et al., 2003; Spero & Lea, 1996).

Table 1
pH Anomalies for the Paleocene-Eocene Thermal Maximum (PETM) and Eocene Thermal Maximum 2 (ETM-2)

	PETM Site 1209 (Pacific)		ETM-2 *A. soldadoensis*		
	M. velascoensis	A. soldadoensis	Site 1210 (Pacific)		Site 1265 (Atlantic)
pH baseline	7.72	7.72	7.78	7.68 (Figure 6)	7.71
pH min	7.41	7.45	7.58	7.43	7.45
ΔpH^a	−0.31 +0.06/−0.06	−0.27 +0.05/−0.06	−0.20 +0.05/−0.05	−0.25 +0.06/−0.07	−0.26 +0.04/−0.05
ΔpH^b	−0.31 +0.14/−0.15	−0.27 +0.13/−0.15	−0.20 +0.12/−0.13	−0.25 +0.14/−0.16	−0.26 +0.12/−0.14

Note. See text for details on reported pH uncertainty. Baseline pH for the PETM is set to 7.72 based on DCESS estimates. When pre-PETM pH of 7.72 is applied to all early Eocene data (i.e., same vital effect offset or *c* value for the PETM and ETM-2), pre-ETM-2 baseline pH = 7.90 for Site 1210. We also include pre-ETM-2 baseline pH = 7.68, which is derived from DCESS-based estimates of long-term pH decline from pre-PETM to pre-ETM-2 (see main text for details).
[a]Uncertainty in anomalies reported as propagated analytical uncertainty in the minimum pH value. [b]Uncertainty in anomalies reported as propagated analytical uncertainty in addition to uncertainty in absolute temperature, salinity, and $\delta^{11}B$ of seawater.

Acarinina and *Morozovella* were symbiont-bearing, so loss or reduction of photosymbionts due to PETM and ETM-2 warming would have lowered their $\delta^{11}B$ and $\delta^{13}C$ values and amplified negative CIEs and inferred acidification. However, peak-CIE SSTs for the PETM and ETM-2 at Site 1209 are ~40 and ~37 °C, respectively, and it is therefore unlikely that mixed-layer foraminifera suffered an equal or higher degree of photosymbiont loss during lesser peak-ETM-2 warmth than during the PETM. Consequently, the large $\delta^{11}B$ shift at ETM-2, and in particular at Site 1265, must be due to other effects.

During the early Eocene, Site 1210 was located within the subtropical North Pacific gyre (Figure 1), where thermal stratification would have been strong and downwelling would have prevailed. Site 1265 was also located in the open ocean, but its location on Walvis Ridge may have caused seasonal shifts in local water mass conditions associated with bathymetrically induced upwelling (e.g., Kucera et al., 1997). Therefore, bottom water influence (i.e., lower pH) on surface waters at Walvis Ridge may have been enhanced during ETM-2 warming (e.g., Jennions et al., 2015). Lower planktic B/Ca at Site 1265 (baseline and peak CIE values) qualitatively supports upwelling at the site (i.e., lower pH and higher DIC would tend to lower B/Ca). Additionally, taking planktic Mg/Ca data at face value, Site 1265 would have been characterized by warmer surface temperatures than Sites 1209/1210 (Figure 4). This is surprising because the higher-latitude location of Site 1265 and modeled early Eocene spatial SST estimates both predict cooler temperatures than at Shatsky Rise (i.e., Dunkley Jones et al., 2013). However, higher peak-CIE Mg/Ca at Site 1265 is consistent with a larger pH (i.e. acidification) influence on Mg/Ca at Site 1265 compared to Sites 1209 and 1210. Once the Mg/Ca data are pH corrected, Site 1265 ETM-2 SSTs better align with those of Site 1209 (Figure 4). Furthermore, the elevated Mg/Ca at Site 1265 may also be driven by upwelling-induced increases in DIC, which tends to increase Mg/Ca in planktic foraminifera shells (e.g., Allen et al., 2016). Therefore, the larger magnitude ocean acidification and higher peak ETM-2 $Mg/Ca_{planktic}$ values at Site 1265 both suggest enhanced upwelling. Thus, we deduce that the −0.20 +0.12/−0.13 pH anomaly of Pacific Site 1210 is more representative of the global change in sea surface pH.

Compared to our $\delta^{11}B$ estimates, our LOSCAR simulations of ETM-2 (2,600 Gt C released over 15, 20, and 25 kyr) generate relatively smaller pH excursions of −0.13 to −0.12, and DCESS with the same fluxes simulates a pH of −0.13 (Figure 5). Consequently, a larger mass of carbon is required to amplify the pH anomaly so that it reaches the magnitude calculated using $\delta^{11}B$ (−0.20). With DCESS, a flux of 3,800 Gt C results in a −0.17 pH decrease (Figure 5), which agrees better with $\delta^{11}B$-based pH estimates (i.e., well within error of −0.20 +0.12/−0.13), but to match the observed CIE requires the carbon have a value of −25‰ (Figure S6), more consistent with an organic source (e.g., Bowen, 2013; DeConto et al., 2012; Kurtz et al., 2003), or possibly some mixture of volcanic and biogenic methane, though a volcanic source is counter to the suggested orbitally triggered mechanism for ETM-2 (e.g., biogenic methane, organic carbon; $\delta^{13}C = -50‰$ to −25‰; i.e., Cramer et al., 2003; DeConto et al., 2012; Lourens et al., 2005; Zeebe & Lourens, 2019).

An even larger mass of carbon would require a more ^{13}C-enriched carbon source to fit within observations of the CIE, for example, a pure volcanic carbon source (~−10‰ $\delta^{13}C$) as asserted by Gutjahr et al. (2017) for the PETM. However, such a massive carbon release is inconsistent with observations of the global CCD (~150 m of shoaling in the Pacific based on sediment records of Leon-Rodriguez & Dickens, 2010, and >35% $CaCO_3$ at

3,600 m paleo-depth along Walvis Ridge maintained during the event; Stap et al., 2009) and magnitude of warming from $\delta^{18}O_{benthic}$, $Mg/Ca_{planktic}$ (2 to 3 °C as constrained by this study), and TEX_{86} (3 to 5 °C; Sluijs et al., 2009), even at a moderate climate sensitivity of 4 °C per CO_2 doubling. For example, with the most extreme DCESS simulation (10,600 Gt C release; Figure S7), the CCD shoals is >500 m, which falls outside estimates for ETM-2. Also, given the 2 to 3 °C rise in temperature, climate sensitivity would need to be more than halved (i.e., <2 °C per CO_2 doubling). Changes in continental weathering and calcification rates can significantly affect the sensitivity of the CCD as argued in Greene et al. (2019) and Boudreau et al. (2018), respectively. However, given current understanding of the two hyperthermal events (i.e., peak SSTs lower for ETM-2 compared with the PETM; Figures 3 and 4; his study; Dunkley Jones et al., 2010), it is unlikely that weathering was amplified to a larger degree during ETM-2 than during the PETM. Similarly, potential decreases in calcification during the PETM, attributed to low-latitude heat-stressed plankton (e.g., Aze et al., 2014), would also likely be less severe during ETM-2.

4.3. Early Eocene pH Paradox?

If we assume little to no change in seawater $\delta^{11}B$ for the study interval, and no change in the vital effects causing the species-specific offset of the $\delta^{11}B_{foram}$ versus $\delta^{11}B_{borate}$ relationship, the planktic foraminifer $\delta^{11}B$-derived pH records require a higher pre-event pH for ETM-2 (i.e., 7.78) than for the PETM (i.e., 7.72; Figures 3 and 4 and Table 1). Our DCESS Earth system model simulations driven by changes in climate (i.e., $\delta^{18}O_{benthic}$) and $\delta^{13}C$ (Figure 2), however, suggest a lower pre-event baseline pH for ETM-2 (i.e., 7.68; Figure 5 and Table S1). Accordingly, we recalculate pH for Site 1210 during ETM-2 using $\delta^{11}B$ following the DCESS-simulated pre-event pH value (i.e., 7.68, rather than the previously used value of 7.78; Figure 6). To obtain an average Site 1210 pre-event (i.e., ETM-2 data > 54.052 Ma) pH of 7.68 requires either changing the $\delta^{11}B_{foram}$ versus $\delta^{11}B_{borate}$ calibration intercept for *A. soldadoensis* from 0.37 to 1.18, or changing ETM-2 $\delta^{11}B_{sw}$ from 38.75‰ to 39.50‰. However, if the vital effect (i.e., the factor controlling the $\delta^{11}B_{foram}$ versus $\delta^{11}B_{borate}$ calibration intercept) changed, $\delta^{13}C_{planktic}$ would likely deviate from long-term $\delta^{13}C$ trends in other carbonates (e.g., benthic and bulk carbonate), which is not the case (Figures 2, 3, and 4). Alternatively, the change in vital effect could have been caused by changes in species-specific boron discrimination, which would influence $\delta^{11}B$, but not $\delta^{13}C$.

The PETM to ETM-2 increase in foraminiferal $\delta^{11}B$ may reflect an increase in $\delta^{11}B_{sw}$, but $\delta^{11}B_{sw}$ is typically thought to change no more than 0.1‰ per Myr (Lemarchand et al., 2000). Paleoenvironmental changes (e.g., enhanced weathering or changes in the deposition of marine sediments) associated with the PETM may have accelerated boron cycling in the oceans. For example, boron removal from seawater via adsorption onto clays or increased crustal alteration may have been enhanced, reducing $[B]_T$ and increasing $\delta^{11}B_{sw}$ (Lemarchand et al., 2000). PETM to ETM-2 decreases in B/Ca (Figures 3 and 4) are consistent with a drop in marine $[B]_T$ over this time interval, suggesting possible reduced boron delivery to the oceans or an enhanced boron sink (i.e., clay adsorption and crustal alteration) from the PETM to ETM-2.

What are the consequences for increased $\delta^{11}B_{sw}$ on reconstructed ETM-2 pH? Increasing $\delta^{11}B_{sw}$ from 38.75‰ to 39.5‰ results in (1) a −0.10 pH unit shift in pre-ETM-2 absolute pH (i.e., from 7.78 to 7.68) and (2) an amplified pH signal across ETM-2 (i.e., $\Delta pH = -0.25\ +0.14/-0.16$ instead of $\Delta pH = -0.20\ +0.12/-0.13$ with a pre-event pH = 7.78; Table 1 and Figure 6). Consequently, the recalculated Site 1210 ETM-2 pH anomaly is more than 0.08 pH units larger in magnitude than the ΔpH generated by our nonvolcanic carbon source simulations, and the difference between the model and proxy observations is even larger than with a baseline pH = 7.78 (Figure 6 and Table 1). Our recalculated proxy-based ΔpH is smaller than but within error of the 10,600 Gt C release DCESS simulation (i.e., ΔpH = −0.38; Figure S7). However, this scenario fails to accurately reproduce observations of warming and is inconsistent with observed $CaCO_3$ dissolution during ETM-2 (Figure S7). Furthermore, the required increase in $\delta^{11}B_{sw}$ is inconsistent with typical rates of $\Delta\delta^{11}B_{sw}$, suggesting additional influences from changing vital effects. In short, replicated $\delta^{11}B$ observations indicate that the pH shifts during ETM-2 were proportionally larger than suggested by observations of the CIE and global warming (assuming nominal climate sensitivity of 4 °C per CO_2 doubling) and by the models parameterized by these CIE and warming observations. This suggests (1) while qualitatively consistent with carbon release and warming, the early Eocene $\delta^{11}B$ data are amplified by effects that have not yet

been calibrated or identified; (2) regional influences came into play at both observational sites; or (3) the models do not yet capture some aspect(s) of early Eocene carbon cycling.

5. Conclusions

We present the first planktic foraminiferal $\delta^{11}B$ data spanning ETM-2 from sites in the Atlantic and Pacific Oceans, which indicate minimum global sea surface acidification of −0.20 +0.12/−0.13. We argue that the North Pacific Site 1210 record is more representative of the global sea surface pH signal due to its paleogeographic location. When pre-PETM pH is set to 7.72, consistent with previous simulations, $\delta^{11}B$ suggests surface pH of 7.78 prior to ETM-2. This is inconsistent with simulations and observations of the long-term decline in $\delta^{13}C$ and warming from the PETM to ETM-2. The decrease in pH during ETM-2 at Site 1210 is amplified to −0.25 +0.14/−0.16 when the pre-ETM-2 pH is set to 7.68, consistent with simulations and observations of long-term early Eocene warming. The computed pH decreases are more than half those estimated for the PETM and exceed estimates based on carbon cycle simulations that constrain carbon fluxes using records of the ETM-2 CCD, ΔSST, and negative $\delta^{13}C$ excursions. To obtain a decrease in pH within the error of the minimum magnitude of surface acidification suggested by $\delta^{11}B$ (i.e., −0.20 +0.12/−0.13), our LOSCAR and DCESS simulations both require a higher carbon flux (i.e., at least double or ≥2,600 Gt C) than previously estimated for ETM-2 (i.e., Harper et al., 2018). Carbon sources depleted in ^{13}C (i.e. biogenic methane with $\delta^{13}C = -50‰$ and/or organic carbon with $\delta^{13}C = -25‰$) are required to achieve this carbon flux (i.e., 2,600 to 3,800 Gt C or a flux consistent with observations of warming and CCD) and stay within the limits of the observed CIE. Our replicated observations (i.e., $\delta^{11}B_{foram}$) indicate that surface ocean pH shifts during ETM-2 were larger than suggested by models. At this point we cannot ascertain the source of this model-data discrepancy, but combined proxy estimates agree that ETM-2 was characterized by a carbon cycle perturbation similar, but not necessarily proportional, to warming and acidification observed at the PETM. The data-model mismatch highlights the need for further scrutiny of both carbon cycle models and boron-based pH estimates.

Acknowledgments
We are grateful to Rob Franks, Colin Carney, and Dyke Andreasen for their analytical support. Thank you to Demir Worthington and Reid Clark for help with sample preparation. This manuscript benefited from discussion with Matthew Clapham, Paul Koch, Donald Penman, and Christina Ravelo. This study was supported by the National Science Foundation (Grants OCE16-57848 to Hönisch and OCE16-58023 to Zachos and Zeebe; OCE15-36611 to Thomas) and the Chilean FONDECYT and Ministry of Economy, Development and Tourism (Grant 1190230 and Millennium Nucleus Paleoclimate grant, both to Shaffer). Reviews from Michael Henehan and one anonymous reviewer greatly improved this manuscript. We appreciate Stephen Barker's editorial handling. This work utilized samples collected as part of the International Ocean Discovery Program (IODP; previously ODP). All data generated as part of this study are available in the supporting information and the PANGAEA database (https://doi.pangaea.de/10.1594/PANGAEA.904063).

References

Abels, H. A., Clyde, W. C., Gingerich, P. D., Hilgen, F. J., Fricke, H. C., Bowen, G. J., & Lourens, L. J. (2012). Terrestrial carbon isotope excursions and biotic change during Palaeogene hyperthermals. *Nature Geoscience*, *5*(5), 326–329. https://doi.org/10.1038/ngeo1427

Allen, K. A., & Hönisch, B. (2012). The planktic foraminiferal B/Ca proxy for seawater carbonate chemistry: A critical evaluation. *Earth and Planetary Science Letters*, *345-348*, 203–211. https://doi.org/10.1016/j.epsl.2012.06.012

Allen, K. A., Hönisch, B., Eggins, S. M., Haynes, L. L., Rosenthal, Y., & Yu, J. (2016). Trace element proxies for surface ocean conditions: A synthesis of culture calibrations with planktic foraminifera. *Geochimica et Cosmochimica Acta*, *193*, 197–221. https://doi.org/10.1016/j.gca.2016.08.015

Allen, K. A., Hönisch, B., Eggins, S. M., Yu, J., Spero, H. J., & Elderfield, H. (2011). Controls on boron incorporation in cultured tests of the planktic foraminifer Orbulina universa. *Earth and Planetary Science Letters*, *309*(3-4), 291–301. https://doi.org/10.1016/j.epsl.2011.07.010

Anagnostou, E., John, E. H., Edgar, K. M., Foster, G. L., Ridgwell, A., Inglis, G. N., et al. (2016). Changing atmospheric CO2 concentration was the primary driver of early Cenozoic climate. *Nature*, *533*(7603), 380–384. https://doi.org/10.1038/nature17423

Anand, P., Elderfield, H., & Conte, M. H. (2003). Calibration of Mg/Ca thermometry in planktonic foraminifera from a sediment trap time series. *Paleoceanography*, *18*(2). https://doi.org/10.1029/2002pa000846

Aze, T., Pearson, P. N., Dickson, A. J., Badger, M. P. S., Bown, P. R., Pancost, R. D., et al. (2014). Extreme warming of tropical waters during the Paleocene-Eocene Thermal Maximum. *Geology*, *42*(9), 739–742. https://doi.org/10.1130/g35637.1

Babila, T. L., Penman, D. E., Honisch, B., Kelly, D. C., Bralower, T. J., Rosenthal, Y., & Zachos, J. C. (2018). Capturing the global signature of surface ocean acidification during the Palaeocene-Eocene Thermal Maximum. *Philosophical Transactions. Series A, Mathematical, Physical, and Engineering Sciences*, *376*(2130). https://doi.org/10.1098/rsta.2017.0072

Babila, T. L., Rosenthal, Y., & Conte, M. H. (2014). Evaluation of the biogeochemical controls on B/Ca of Globigerinoides ruber white from the Oceanic Flux Program, Bermuda. *Earth and Planetary Science Letters*, *404*, 67–76. https://doi.org/10.1016/j.epsl.2014.05.053

Babila, T. L., Rosenthal, Y., Wright, J. D., & Miller, K. G. (2016). A continental shelf perspective of ocean acidification and temperature evolution during the Paleocene-Eocene Thermal Maximum. *Geology*, *44*(4), 275–278. https://doi.org/10.1130/g37522.1

Baczynski, A. A., McInerney, F. A., Wing, S. L., Kraus, M. J., Bloch, J. I., & Secord, R. (2017). Constraining paleohydrologic change during the Paleocene-Eocene Thermal Maximum in the continental interior of North America. *Palaeogeography, Palaeoclimatology, Palaeoecology*, *465*, 237–246. https://doi.org/10.1016/j.palaeo.2016.10.030

Barker, S., Greaves, M., & Elderfield, H. (2003). A study of cleaning procedures used for foraminiferal Mg/Ca paleothermometry, *Geochemistry, Geophysics. Geosystems*, *4*(9), 20. https://doi.org/10.1029/2003gc000559

Barnet, J. S. K., Littler, K., Westerhold, T., Kroon, D., Leng, M. J., Bailey, I., et al. (2019). A high-fidelity benthic stable isotope record of Late Cretaceous-Early Eocene climate change and carbon-cycling. *Paleoceanography and Paleoclimatology*. https://doi.org/10.1029/2019pa003556

Bijl, P. K., Schouten, S., Sluijs, A., Reichart, G. J., Zachos, J. C., & Brinkhuis, H. (2009). Early Palaeogene temperature evolution of the southwest Pacific Ocean. *Nature*, *461*(7265), 776–779. https://doi.org/10.1038/nature08399

Boudreau, B. P., Middelburg, J. J., & Luo, Y. (2018). The role of calcification in carbonate compensation. *Nature Geoscience*, *11*(12), 894–900. https://doi.org/10.1038/s41561-018-0259-5

Bowen, G. J. (2013). Up in smoke: A role for organic carbon feedbacks in Paleogene hyperthermals. *Global and Planetary Change*, *109*, 18–29. https://doi.org/10.1016/j.gloplacha.2013.07.001

Bralower, T. J., Premoli-Silva, I., Malone, M. J., & Party, L. S. S. (2002). *Proceedings of the Ocean Drilling Program, Initial Reports* (Vol. 198). College Station, TX, USA: Ocean Drilling Program.

Brown, R. E., Anderson, L. D., Thomas, E., & Zachos, J. C. (2011). A core-top calibration of B/Ca in the benthic foraminifers Nuttallides umbonifera and Oridorsalis umbonatus: A proxy for Cenozoic bottom water carbonate saturation. *Earth and Planetary Science Letters*, *310*(3-4), 360–368. https://doi.org/10.1016/j.epsl.2011.08.023

Colosimo, A. B., Bralower, T. J., & Zachos, J. C. (2006). Evidence for lysocline shoaling at the Paleocene/Eocene thermal maximum on Shatsky Rise, Northwest Pacific. In *Proceedings of the Ocean Drilling Program, Scientific Results* (Vol. 198, pp. 1–36). College Station, TX, USA: Ocean Drilling Program.

Cramer, B. S., Wright, J. D., Kent, D. V., & Aubry, M.-P. (2003). Orbital climate forcing of δ13C excursions in the late Paleocene-early Eocene (chrons C24n-C25n). *Paleoceanography*, *18*(4). https://doi.org/10.1029/2003pa000909

D'Ambrosia, A. R., Clyde, W. C., Fricke, H. K., Gingerich, P. D., & Abels, H. A. (2017). Repetitive mammalian dwarfing during ancient greenhouse warming events. *Science Advances*, *3*, 9. https://doi.org/10.1126/sciadv.1601430

D'Hondt, S., Zachos, J. C., & Schultz, G. (1994). Stable isotope signals and photosymbiosis in Late Paleocene Planktic Foraminifera. *Paleobiology*, *20*(3), 16. https://doi.org/10.1017/s0094837300012847

DeConto, R. M., Galeotti, S., Pagani, M., Tracy, D., Schaefer, K., Zhang, T., et al. (2012). Past extreme warming events linked to massive carbon release from thawing permafrost. *Nature*, *484*(7392), 87–91. https://doi.org/10.1038/nature10929

Dickens, G. R., O'Neil, J. R., Rea, D. K., & Owen, R. M. (1995). Dissociation of oceanic methane hydrate as a cause of the carbon isotope excursion at the end of the Paleocene. *Paleoceanography*, *10*(6), 7. https://doi.org/10.1029/95pa02087

Dunkley Jones, T., Lunt, D. J., Schmidt, D. N., Ridgwell, A., Sluijs, A., Valdes, P. J., & Maslin, M. (2013). Climate model and proxy data constraints on ocean warming across the Paleocene-Eocene Thermal Maximum. *Earth-Science Reviews*, *125*, 123–145. https://doi.org/10.1016/j.earscirev.2013.07.004

Dunkley Jones, T., Ridgwell, A., Lunt, D. J., Maslin, M. A., Schmidt, D. N., & Valdes, P. J. (2010). A Palaeogene perspective on climate sensitivity and methane hydrate instability. *Philosophical Transactions. Series A, Mathematical, Physical, and Engineering Sciences*, *368*(1919), 2395–2415. https://doi.org/10.1098/rsta.2010.0053

Dyez, K. A., Hönisch, B., & Schmidt, G. A. (2018). Early pleistocene obliquity-scale pCO_2 variability at ~1.5 million years ago. *Paleoceanography and Paleoclimatology*, *33*(11), 1270–1291. https://doi.org/10.1029/2018pa003349

Edgar, K. M., Anagnostou, E., Pearson, P. N., & Foster, G. L. (2015). Assessing the impact of diagenesis on $\delta^{11}B$, $\delta^{13}C$, $\delta^{18}O$, Sr/Ca and B/Ca values in fossil planktic foraminiferal calcite. *Geochimica et Cosmochimica Acta*, *166*, 189–209. https://doi.org/10.1016/j.gca.2015.06.018

Evans, D., & Müller, W. (2012). Deep time foraminifera Mg/Ca paleothermometry: Nonlinear correction for secular change in seawater Mg/Ca. *Paleoceanography*, *27*(4). https://doi.org/10.1029/2012pa002315

Evans, D., Sagoo, N., Renema, W., Cotton, L. J., Müller, W., Todd, J. A., et al. (2018). Eocene greenhouse climate revealed by coupled clumped isotope-Mg/Ca thermometry. *Proceedings of the National Academy of Sciences of the United States of America*, *115*(6), 1174–1179. https://doi.org/10.1073/pnas.1714744115

Evans, D., Wade, B. S., Henehan, M., Erez, J., & Müller, W. (2016). Revisiting carbonate chemistry controls on planktic foraminifera Mg/Ca: Implications for sea surface temperature and hydrology shifts over the Paleocene–Eocene Thermal Maximum and Eocene–Oligocene transition. *Climate of the Past*, *12*(4), 819–835. https://doi.org/10.5194/cp-12-819-2016

Foster, G. L., Hönisch, B., Paris, G., Dwyer, G. S., Rae, J. W. B., Elliott, T., et al. (2013). Interlaboratory comparison of boron isotope analyses of boric acid, seawater and marine $CaCO_3$ by MC-ICPMS and NTIMS. *Chemical Geology*, *358*, 1–14. https://doi.org/10.1016/j.chemgeo.2013.08.027

Gibbs, S. J., Bown, P. R., Murphy, B. H., Sluijs, A., Edgar, K. M., Pälike, H., et al. (2012). Scaled biotic disruption during early Eocene global warming events. *Biogeosciences*, *9*(11), 4679–4688. https://doi.org/10.5194/bg-9-4679-2012

Greene, S. E., Ridgwell, A., Kirtland Turner, S., Schmidt, D. N., Palike, H., Thomas, E., et al. (2019). Early Cenozoic decoupling of climate and carbonate compensation depth trends. *Paleoceanography and Paleoclimatology*, *34*(6), 930–945. https://doi.org/10.1029/2019PA003601

Gutjahr, M., Ridgwell, A., Sexton, P. F., Anagnostou, E., Pearson, P. N., Palike, H., et al. (2017). Very large release of mostly volcanic carbon during the Palaeocene-Eocene Thermal Maximum. *Nature*, *548*(7669), 573–577. https://doi.org/10.1038/nature23646

Hain, M. P., Sigman, D. M., Higgins, J. A., & Haug, G. H. (2015). The effects of secular calcium and magnesium concentration changes on the thermodynamics of seawater acid/base chemistry: Implications for Eocene and Cretaceous ocean carbon chemistry and buffering. *Global Biogeochemical Cycles*, *29*(5), 517–533. https://doi.org/10.1002/2014gb004986

Harper, D. T., Zeebe, R., Hönisch, B., Schrader, C. D., Lourens, L. J., & Zachos, J. C. (2018). Subtropical sea-surface warming and increased salinity during Eocene Thermal Maximum 2. *Geology*, *46*(2), 187–190. https://doi.org/10.1130/g39658.1

Haynes, L. L., Hönisch, B., Dyez, K. A., Holland, K., Rosenthal, Y., Fish, C. R., et al. (2017). Calibration of the B/Ca proxy in the planktic foraminifer Orbulina universa to Paleocene seawater conditions. *Paleoceanography*, *32*(6), 580–599. https://doi.org/10.1002/2016PA003069

Hemming, N. G., & Hanson, G. N. (1992). Boron isotopic composition and concentration in modern marine carbonates. *Geochimica et Cosmochimica Acta*, *56*, 7. https://doi.org/10.1016/0016-7037(92)90151-8

Henehan, M. J., Foster, G. L., Bostock, H. C., Greenop, R., Marshall, B. J., & Wilson, P. A. (2016). A new boron isotope-pH calibration for Orbulina universa, with implications for understanding and accounting for 'vital effects'. *Earth and Planetary Science Letters*, *454*, 282–292. https://doi.org/10.1016/j.epsl.2016.09.024

Henehan, M. J., Foster, G. L., Rae, J. W. B., Prentice, K. C., Erez, J., Bostock, H. C., et al. (2015). Evaluating the utility of B/Ca ratios in planktic foraminifera as a proxy for the carbonate system: A case study of Globigerinoides ruber, *Geochemistry, Geophysics. Geosystems*, *16*(4), 1052–1069. https://doi.org/10.1002/2014GC005514

Hershey, J. P., Fernandez, M., Milne, P. J., & Millero, F. J. (1986). The ionization of boric acid in NaCl, Na-Ca-Cl and Na-Mg-Cl solutions at 25C. *Geochimica et Cosmochimica Acta*, *50*, 6. https://doi.org/10.1016/0016-7037(86)90059-1

Hönisch, B., Bijma, J., Russell, A. D., Spero, H. J., Palmer, M. R., Zeebe, R. E., & Eisenhauer, A. (2003). The influence of symbiont photosynthesis on the boron isotopic composition of foraminifera shells. *Marine Micropaleontology*, *49*(1-2), 87–96. https://doi.org/10.1016/s0377-8398(03)00030-6

Hönisch, B., Hemming, N. G., Archer, D., Siddall, M., & McManus, J. F. (2009). Atmospheric carbon dioxide concentration across the mid-Pleistocene transition. *Science*, *324*(5934), 1551–1554. https://doi.org/10.1126/science.1171477

Hönisch, B. r., Eggins, S. M., Haynes, L. L., Allen, K. A., Holland, K., & Lorbacher, K. (2019). *Boron proxies in paleoceanography and paleoclimatology*. West Sussex, UK: John Wiley & Sons Ltd.

Huber, M., & Caballero, R. (2003). Eocene El Niño: Evidence for robust tropical dynamics in the "Hothouse". *Science*, *299*, 5. https://doi.org/10.1126/science.1078766

Jagniecki, E. A., Lowenstein, T. K., Jenkins, D. M., & Demicco, R. V. (2015). Eocene atmospheric CO2 from the nahcolite proxy. *Geology*. https://doi.org/10.1130/g36886.1

Jennions, S. M., Thomas, E., Schmidt, D. N., Lunt, D., & Ridgwell, A. (2015). Changes in benthic ecosystems and ocean circulation in the Southeast Atlantic across Eocene Thermal Maximum 2. *Paleoceanography*, *30*(8), 1059–1077. https://doi.org/10.1002/2015pa002821

Kennett, J. P., & Stott, L. D. (1991). Abrupt deep-sea warming, palaeoceanographic changes and benthic extinctions at the end of the Palaeocene. *Nature*, *353*. https://doi.org/10.1038/353225a0

Kiehl, J. T., & Shields, C. A. (2013). Sensitivity of the Palaeocene-Eocene Thermal Maximum climate to cloud properties. *Philosophical Transactions. Series A, Mathematical, Physical, and Engineering Sciences*, *371*(2001), 20130093. https://doi.org/10.1098/rsta.2013.0093

Kirtland Turner, S., & Ridgwell, A. (2016). Development of a novel empirical framework for interpreting geological carbon isotope excursions, with implications for the rate of carbon injection across the PETM. *Earth and Planetary Science Letters*, *435*, 1–13. https://doi.org/10.1016/j.epsl.2015.11.027

Klochko, K., Kaufman, A. J., Yao, W., Byrne, R. H., & Tossell, J. A. (2006). Experimental measurement of boron isotope fractionation in seawater. *Earth and Planetary Science Letters*, *248*(1-2), 276–285. https://doi.org/10.1016/j.epsl.2006.05.034

Koch, P. L., Zachos, J. C., & Gingerich, P. D. (1992). Correlation between isotope records in marine and continental carbon reservoirs near the Palaeocene/Eocene boundary. *Nature*, *358*. https://doi.org/10.1038/358319a0

Komar, N., Zeebe, R. E., & Dickens, G. R. (2013). Understanding long-term carbon cycle trends: The late Paleocene through the early Eocene. *Paleoceanography*, *28*(4), 650–662. https://doi.org/10.1002/palo.20060

Kozdon, R., Kelly, D. C., Kitajima, K., Strickland, A., Fournelle, J. H., & Valley, J. W. (2013). In situ $\delta^{18}O$ and Mg/Ca analyses of diagenetic and planktic foraminiferal calcite preserved in a deep-sea record of the Paleocene-Eocene thermal maximum. *Paleoceanography*, *28*(3), 517–528. https://doi.org/10.1002/palo.20048

Kraus, M. J., & Riggins, S. (2007). Transient drying during the Paleocene-Eocene Thermal Maximum (PETM): Analysis of paleosols in the bighorn basin, Wyoming, *Palaeogeography, Palaeoclimatology. Palaeoecology*, *245*(3-4), 444–461. https://doi.org/10.1016/j.palaeo.2006.09.011

Kucera, M., Malmgren, B. A., & Sturesson, U. (1997). Foraminiferal dissolution at the shallow depths of the Walvis Ridge and Rio Grande Rise during the latest Cretaceous: Inferences for deep-water circuation in the South Atlantic. *Palaeogeography, Palaeoclimatology, Palaeoecology*, *129*, 18. https://doi.org/10.1016/s0031-0182(96)00133-2

Kurtz, A. C., Kump, L. R., Arthur, M. A., Zachos, J. C., & Paytan, A. (2003). Early Cenozoic decoupling of the global carbon and sulfur cycles. *Paleoceanography*, *18*(4). https://doi.org/10.1029/2003pa000908

Lemarchand, D., Gaillardet, J., Lewin, E., & Allegre, C. J. (2000). The influence of rivers on marine boron isotopes and implications for reconstructing past ocean pH. *Nature*, *408*(21/28), 951–954. https://doi.org/10.1038/35050058

Leon-Rodriguez, L., & Dickens, G. R. (2010). Constraints on ocean acidification associated with rapid and massive carbon injections: The early Paleogene record at ocean drilling program site 1215, equatorial Pacific Ocean, *Palaeogeography, Palaeoclimatology. Palaeoecology*, *298*(3-4), 409–420. https://doi.org/10.1016/j.palaeo.2010.10.029

Littler, K., Röhl, U., Westerhold, T., & Zachos, J. C. (2014). A high-resolution benthic stable-isotope record for the South Atlantic: Implications for orbital-scale changes in Late Paleocene–Early Eocene climate and carbon cycling. *Earth and Planetary Science Letters*, *401*, 18–30. https://doi.org/10.1016/j.epsl.2014.05.054

Lourens, L. J., Sluijs, A., Kroon, D., Zachos, J. C., Thomas, E., Rohl, U., et al. (2005). Astronomical pacing of late Palaeocene to early Eocene global warming events. *Nature*, *435*(7045), 1083–1087. https://doi.org/10.1038/nature03814

Luciani, V., D'Onofrio, R., Dickens, G. R., & Wade, B. S. (2017). Planktic foraminiferal response to early Eocene carbon cycle perturbations in the southeast Atlantic Ocean (ODP Site 1263). *Global and Planetary Change*, *158*, 119–133. https://doi.org/10.1016/j.gloplacha.2017.09.007

Martin, P. A., & Lea, D. W. (2002). A simple evaluation of cleaning procedures on fossil benthic foraminiferal Mg/Ca, *Geochemistry, Geophysics. Geosystems*, *3*(10), 1–8. https://doi.org/10.1029/2001gc000280

Matsumoto, K. (2007). Biology-mediated temperature control on atmospheric pCO_2 and ocean biogeochemistry. *Geophysical Research Letters*, *34*(20). https://doi.org/10.1029/2007gl031301

Matthews, K. J., Maloney, K. T., Zahirovic, S., Williams, S. E., Seton, M., & Müller, R. D. (2016). Global plate boundary evolution and kinematics since the late Paleozoic. *Global and Planetary Change*, *146*, 226–250. https://doi.org/10.1016/j.gloplacha.2016.10.002

McCarren, H. K. (2009). *Paleoceanographic variability of extreme climates in the early Paleogene, 196 pp*. Santa Cruz: University of California.

Millero, F. J. (1995). Thermodynamics of the carbon dioxide system in the oceans. *Geochimica et Cosmochimica Acta*, *59*(4), 16. https://doi.org/10.1016/0016-7037(94)00354-o

Nicolo, M. J., Dickens, G. R., Hollis, C. J., & Zachos, J. C. (2007). Multiple early Eocene hyperthermals: Their sedimentary expression on the New Zealand continental margin and in the deep sea. *Geology*, *35*(8). https://doi.org/10.1130/g23648a.1

Penman, D. E., Hönisch, B., Zeebe, R. E., Thomas, E., & Zachos, J. C. (2014). Rapid and sustained surface ocean acidification during the Paleocene-Eocene Thermal Maximum. *Paleoceanography*, *29*(5), 357–369. https://doi.org/10.1002/2014pa002621

Pérez-Díaz, L., & Eagles, G. (2018). Estimating palaeobathymetry with quantified uncertainties: a workflow illustrated with South Atlantic data. *Geological Society, London, Special Publications*. https://doi.org/10.1144/sp476.1

Petrizzo, M. R. (2007). The onset of the Paleocene-Eocene Thermal Maximum (PETM) at Sites 1209 and 1210 (Shatsky Rise, Pacific Ocean) as recorded by planktonic foraminifera. *Marine Micropaleontology*, *63*(3-4), 187–200. https://doi.org/10.1016/j.marmicro.2006.11.007

Raffi, I., Backman, J., Zachos, J. C., & Sluijs, A. (2009). The response of calcareous nannofossil assemblages to the Paleocene Eocene Thermal Maximum at the Walvis Ridge in the South Atlantic. *Marine Micropaleontology*, *70*(3-4), 201–212. https://doi.org/10.1016/j.marmicro.2008.12.005

Röhl, U., Westerhold, T., Bralower, T. J., & Zachos, J. C. (2007). On the duration of the Paleocene-Eocene thermal maximum (PETM), *Geochemistry, Geophysics. Geosystems*, *8*(12). https://doi.org/10.1029/2007gc001784

Salmon, K. H., Anand, P., Sexton, P. F., & Conte, M. (2016). Calcification and growth processes in planktonic foraminifera complicate the use of B/Ca and U/Ca as carbonate chemistry proxies. *Earth and Planetary Science Letters*, *449*, 372–381. https://doi.org/10.1016/j.epsl.2016.05.016

Sanyal, A., Bijma, J., Spero, H., & Lea, D. W. (2001). Empirical relationship between pH and the boron isotopic composition ofGlobigerinoides sacculifer: Implications for the boron isotope paleo-pH proxy. *Paleoceanography*, *16*(5), 515–519. https://doi.org/10.1029/2000pa000547

Schmitz, B., & Pujalte, V. (2007). Abrupt increase in seasonal extreme precipitation at the Paleocene-Eocene boundary. *Geology*, *35*(3). https://doi.org/10.1130/g23261a.1

Shaffer, G., Huber, M., Rondanelli, R., & Pepke Pedersen, J. O. (2016). Deep time evidence for climate sensitivity increase with warming. *Geophysical Research Letters*, *43*(12), 6538–6545. https://doi.org/10.1002/2016gl069243

Shaffer, G., Malskær Olsen, S., & Pepke Pedersen, J. O. (2008). Presentation, calibration and validation of the low-order, DCESS Earth System Model (Version 1). *Geoscientific Model Development*, *1*(1), 17–51. https://doi.org/10.5194/gmd-1-17-2008

Slotnick, B. S., Lauretano, V., Backman, J., Dickens, G. R., Sluijs, A., & Lourens, L. (2015). Early Paleogene variations in the calcite compensation depth: New constraints using old borehole sediments from across Ninetyeast Ridge, central Indian Ocean. *Climate of the Past*, *11*(3), 473–493. https://doi.org/10.5194/cp-11-473-2015

Sluijs, A., & Brinkhuis, H. (2009). A dynamic climate and ecosystem state during the Paleocene-Eocene Thermal Maximum: Inferences from dinoflagellate cyst assemblages on the New Jersey Shelf. *Biogeosciences*, *6*, 26. https://doi.org/10.5194/bg-6-1755-2009

Sluijs, A., Brinkhuis, H., Schouten, S., Bohaty, S. M., John, C. M., Zachos, J. C., et al. (2007). Environmental precursors to rapid light carbon injection at the Palaeocene/Eocene boundary. *Nature*, *450*(7173), 1218–1221. https://doi.org/10.1038/nature06400

Sluijs, A., Schouten, S., Donders, T. H., Schoon, P. L., Röhl, U., Reichart, G. J., et al. (2009). Warm and wet conditions in the Arctic region during Eocene Thermal Maximum 2. *Nature Geoscience*, *2*. https://doi.org/10.1038/NGE0668

Spero, H. J., & Lea, D. W. (1996). Experimental determination of stable isotope variability in *Globigerina bulloides*: Implications for paleoceanographic reconstructions. *Marine Micropaleontology*, *28*, 15. https://doi.org/10.1016/0377-8398(96)00003-5

Stap, L., Lourens, L., van Dijk, A., Schouten, S., & Thomas, E. (2010). Coherent pattern and timing of the carbon isotope excursion and warming during Eocene Thermal Maximum 2 as recorded in planktic and benthic foraminifera. *Geochemistry, Geophysics, Geosystems*, *11*(11). https://doi.org/10.1029/2010gc003097

Stap, L., Lourens, L. J., Thomas, E., Sluijs, A., Bohaty, S., & Zachos, J. C. (2010). High-resolution deep-sea carbon and oxygen isotope records of Eocene Thermal Maximum 2 and H2. *Geology*, *38*(7), 607–610. https://doi.org/10.1130/g30777.1

Stap, L., Sluijs, A., Thomas, E., & Lourens, L. (2009). Patterns and magnitude of deep sea carbonate dissolution during Eocene Thermal Maximum 2 and H2, Walvis Ridge, southeastern Atlantic Ocean. *Paleoceanography*, *24*(1). https://doi.org/10.1029/2008pa001655

Takeda, K., & Kaiho, K. (2007). Faunal turnovers in central Pacific benthic foraminifera during the Paleocene-Eocene thermal maximum, *Palaeogeography, Palaeoclimatology*. *Palaeoecology*, *251*(2), 175–197. https://doi.org/10.1016/j.palaeo.2007.02.026

Thomas, E., & Shackleton, N. J. (1996). The Paleocene-Eocene benthic foraminiferal extinction and stable isotope anomalies. *Geological Society, London, Special Publications*, *101*(1), 401–441. https://doi.org/10.1144/gsl.Sp.1996.101.01.20

van Hinsbergen, D. J., de Groot, L. V., van Schaik, S. J., Spakman, W., Bijl, P. K., Sluijs, A., et al. (2015). A paleolatitude calculator for paleoclimate studies. *PLoS ONE*, *10*(6), e0126946. https://doi.org/10.1371/journal.pone.0126946

Westerhold, T., Röhl, U., Donner, B., McCarren, H. K., & Zachos, J. C. (2011). A complete high-resolution Paleocene benthic stable isotope record for the central Pacific (ODP Site 1209). *Paleoceanography*, *26*(2). https://doi.org/10.1029/2010pa002092

Westerhold, T., Röhl, U., Donner, B., & Zachos, J. C. (2018). Global Extent of Early Eocene Hyperthermal Events: A New Pacific Benthic Foraminiferal Isotope Record From Shatsky Rise (ODP Site 1209). *Paleoceanography and Paleoclimatology*, *33*(6), 626–642. https://doi.org/10.1029/2017pa003306

Westerhold, T., Röhl, U., Frederichs, T., Agnini, C., Raffi, I., Zachos, J. C., & Wilkens, R. H. (2017). Astronomical calibration of the Ypresian timescale: Implications for seafloor spreading rates and the chaotic behavior of the solar system? *Climate of the Past*, *13*(9), 1129–1152. https://doi.org/10.5194/cp-13-1129-2017

Yu, J., Elderfield, H., & Hönisch, B. (2007). B/Ca in planktonic foraminifera as a proxy for surface seawater pH. *Paleoceanography*, *22*(2). https://doi.org/10.1029/2006pa001347

Zachos, J. C., Kroon, D. C., Blum, P., Bowles, J., Gaillot, P., Hasegawa, T., et al. (2004). *Proceedings of the Ocean Drilling Program*, (Vol. *208*, Initial Reports). Early Cenozoic Extreme Climates: The Walvis Ridge Transect.

Zachos, J. C., Pagani, M., Sloan, L., Thomas, E., & Billups, K. (2001). Trends, rhythms, and aberrations in global climate 65 Ma to present. *Science*, *292*(5517), 686–693. https://doi.org/10.1126/science.1059412

Zachos, J. C., Röhl, U., Schellenberg, S. A., Sluijs, A., Hodell, D. A., Kelly, D. C., et al. (2005). Rapid acidification of the ocean during the Paleocene-Eocene thermal maximum. *Science*, *308*(5728), 1611–1615. https://doi.org/10.1126/science.1109004

Zachos, J. C., Wara, M. W., Bohaty, S., Delaney, M. L., Petrizzo, M. R., Brill, A., et al. (2003). A Transient rise in tropical sea surface temperature during the Paleocene-Eocene Thermal Maximum. *Science*, *302*. https://doi.org/10.1126/science.1090110

Zeebe, R., & Lourens, L. (2019). Solar System chaos and the Paleocene-Eocene boundary age constrained by geology and astronomy. *Science*, *365*(6456), 4. https://doi.org/10.1126/science.aax0612

Zeebe, R. E. (2012). LOSCAR: Long-term Ocean-atmosphere-Sediment CArbon cycle Reservoir Model v2.0.4. *Geoscientific Model Development*, *5*(1), 149–166. https://doi.org/10.5194/gmd-5-149-2012

Zeebe, R. E. (2013). What caused the long duration of the Paleocene-Eocene Thermal Maximum? *Paleoceanography*, *28*(3), 440–452. https://doi.org/10.1002/palo.20039

Zeebe, R. E., & Tyrrell, T. (2019). History of carbonate ion concentration over the last 100 million years II: Revised calculations and new data. *Geochimica et Cosmochimica Acta*, *257*, 373–392. https://doi.org/10.1016/j.gca.2019.02.041

Zeebe, R. E., Westerhold, T., Littler, K., & Zachos, J. C. (2017). Orbital forcing of the Paleocene and Eocene carbon cycle. *Paleoceanography*, *32*(5), 440–465. https://doi.org/10.1002/2016pa003054

Zeebe, R. E., & Wolf-Gladrow, D. (2001). *CO_2 in seawater: Equilibrium, Kinetics, Isotopes*. Amsterdam, The Netherlands: Elsevier Science B.V.

Zeebe, R. E., Zachos, J. C., & Dickens, G. R. (2009). Carbon dioxide forcing alone insufficient to explain Palaeocene-Eocene Thermal Maximum warming. *Nature Geoscience*, *2*(8), 576–580. https://doi.org/10.1038/ngeo578